J. Fluid Mech. (1985), *vol.* 159, *pp.* 19–53
Printed in Great Britain

Internal solitons on the pycnocline: generation, propagation, and shoaling and breaking over a slope

By TIMOTHY W. KAO, FUH-SHING PAN AND DOMINIQUE RENOUARD†
Department of Civil Engineering, The Catholic University of America, Washington, D.C. 20064

(Received 25 June 1984 and in revised form 4 March 1985)

In Part 1 a study is made of the internal solitary wave on the pycnocline of a continuously stratified fluid. A Korteweg–de Vries (KdV) equation for the 'interfacial' displacement is developed following Benney's method for long nonlinear waves. Experiments were conducted in a long wave tank with the pycnocline at several different depths below the free surface, while keeping the total depth approximately constant. A step-like pool of light water, trapped behind a sliding gate, served as the initial disturbance condition. The number of solitons generated was verified to satisfy the prediction of inverse-scattering theory. The fully developed soliton was found to satisfy the KdV theory for all ratios of upper-layer thickness to total depth.

In Part 2 of this study we investigate experimentally the evolution and breaking of an internal solitary wave as it shoals on a sloping bottom connecting the deeper region where the waves were generated to a shallower shelf region. It is found through quantitative measurements that the onset of wave-breaking was governed by shear instability, which was initiated when the local gradient Richardson number became less than $\frac{1}{4}$. The internal solitary wave of depression was found to steepen at the back of the wave before breaking, in contrast with waves of elevation. Two slopes were used, with ratios 1:16 and 1:9, and the fluid was a Boussinesq fluid with weak stratification using brine solutions.

Preliminary remarks

Trains of internal solitary waves of very large amplitudes ($\sim$60 m) were quantitatively documented by Osborne and others in 1976 in the Andaman Sea (see Osborne & Burch 1980) in water of total depth of over 1000 m. The waves have maximum amplitude at the midthermocline level located at approximately 150 m below the free surface. Observations of similar waves have also been reported by Apel (1981) in the Sulu Sea from satellite pictures, and others have reported them to be present in the Straits of Gibraltar, in the Gulf of Maine and other regions of the world's coastal oceans. The waves in the Andaman Sea and in the Sulu Sea are known to dissipate in the shoaling region along the coast.

In the present paper we study the generation, propagation, attenuation, shoaling and breaking of the internal solitary waves on the pycnocline, for a continuously stratified fluid of the 'thermocline' type, principally through laboratory experiments, complemented where applicable by theoretical considerations. The generation, initial

† Permanent address: Institut de Mécanique de Grenoble, France.

breaking and propagation are first studied in water of constant total depth, and the results presented in Part 1. The shoaling, breaking, reflection and transmission are presented in Part 2.

PART 1. THE KdV THEORY AND ITS VERIFICATION

1. Introduction

Internal solitary waves in a two-layered fluid of constant total depth have been studied by Keulegan (1953), Long (1956, 1965) and Benjamin (1966), and laboratory experiments have recently been undertaken by Koop & Butler (1981) for two immiscible fluid layers with a large density difference. A limited number of experiments, using a similar type of stratification as the present study, have also been reported by Segur & Hammack (1982). In this part of the paper we describe a laboratory method for the generation of internal solitary waves on the pycnocline whereby the amplitude and the number of waves can be easily controlled and predetermined. Initial breaking in the formation region of the waves is discussed. The number of waves generated are checked against inverse-scattering theory. The wave speed and form distribution of the wave so generated are measured by hot-film anemometry and an 'interface follower', and compared with theoretical results. The theoretical results are derived using a hyperbolic-tangent or 'thermocline' type density stratification, from a method introduced by Benney (1966). The method leads to the Korteweg–de Vries (KdV) equation as the evolution equation of the internal-wave modes, of which the lowest mode is of the greatest interest. For the lowest mode the KdV equation for the displacement of the interfacial isopycnic is obtained. It is shown that, in the limit of zero pycnocline thickness, the conventional two-layer model, used by previous authors, is recovered. On the other hand, for finite pycnocline thicknesses, the quantitative results are substantially different from those of the two-layered model for all important wave parameters. The experimental results are given for the lowest internal mode for a number of *nominal* thickness ratios between the upper and lower layers, ranging from approximately 1:4 to 1:36.† It will be shown that for all thickness ratios the waveform is described by the sech^2 distribution of the KdV theory, and the wavelength *vs.* amplitude and the wave-speed *vs.* amplitude relationships of the KdV theory are satisfied uniformly to a good degree of precision.

2. Theoretical aspects

The theoretical model we use is based on a method developed by Benney (1966) to study long finite-amplitude waves. The method is applied to a fluid of finite total depth D, with a hyperbolic-tangent density profile, or 'thermocline' profile, defined as

$$\rho(z) = \rho_0(1 - \varpi \tanh \alpha z), \tag{1}$$

† It should be noted that when one layer is infinitely deep a different scaling law and an equation different from the KdV equation have been proposed by Benjamin (1967). The governing equation is known in the literature as the Benjamin–Ono (BO) equation. The waveform follows a Lorentzian distribution. Theoretical models known as 'finite-depth' models have also been proposed by others when one layer is much deeper than the other. These latter models are essentially small perturbations of the BO model and are singular in the KdV limit. The scaling laws and waveform profiles from all these models have never been confirmed experimentally.

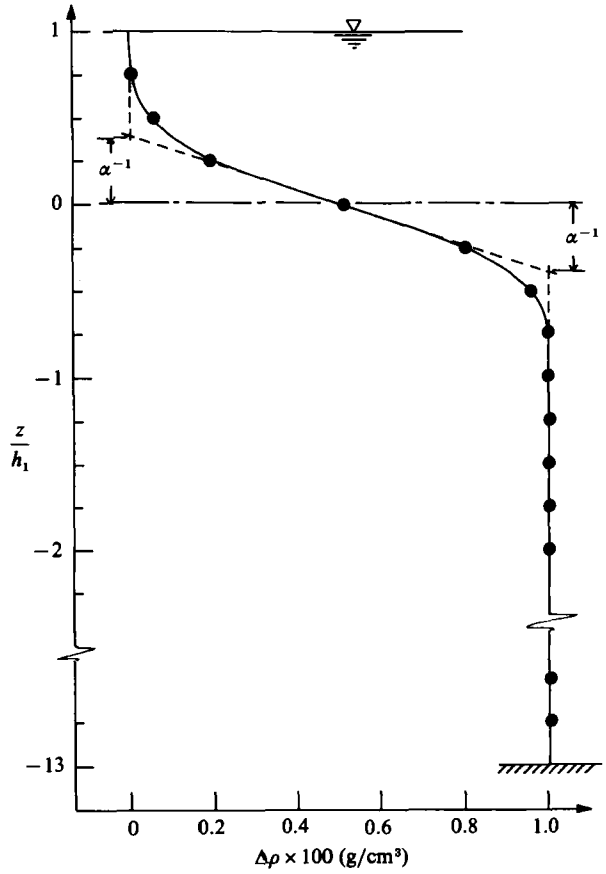

FIGURE 1. Typical density profile measured by conductivity probe.

where $\rho_0 = \frac{1}{2}(\rho_1+\rho_2)$, $\varpi = (\rho_2-\rho_1)/2\rho_0$ (ρ_1 and ρ_2 being respectively the densities of the upper and lower layers), z is the vertical coordinate, the origin of which is located at the midpycnocline, or interface, level, and α^{-1} is a representative half-depth of the pycnocline as shown in figure 1. The nominal thicknesses h_1 and h_2 of the upper and lower layers respectively are defined from this interface level, and the upper ($z = h_1$) and lower ($z = -h_2$) boundaries are assumed to be rigid.

The basic idea is to look for a stream function written as a power series in two small parameters, which are equated through the basic KdV scaling law relating the amplitude to the wavelength; in other words, the characteristic wavelength varies inversely as the square root of the wave amplitude. To first order in ϵ (the wave amplitude normalized by D) a KdV equation is obtained. For a continuous stratification the problem reduces to finding the solution of the modal function $\phi(z)$ at the zeroth order in both small parameters, from the zeroth-order eigenvalue problem given by

$$(\bar{\rho}\phi_z)_z - \frac{g\bar{\rho}_z}{c_0^2}\phi = 0, \quad \phi(h_1) = \phi(-h_2) = 0, \tag{2}$$

where the subscripts denote differentiation, g is the acceleration due to gravity and c_0 is the zeroth-order (i.e. linear) wave speed. The eigenvalue problem admits a denumerably infinite set of eigenfunctions and corresponding eigenvalue $(c_0)_n$. The

Case (mode 1)	r	$s/\tilde{c}_0$	c_0 (cm/s)	Two-layer c_0 (cm/s)
$h_1/D = \frac{1}{14}$				
$\alpha D = 56$	−9.0552	−0.0129	4.526	
$\alpha D = 28$	−7.0621	−0.0152	4.323	4.791
$h_1/D = \frac{2}{14}$				
$\alpha D = 56$	−4.3011	−0.0220	6.314	
$\alpha D = 28$	−4.1538	−0.0236	6.096	6.513
$h_1/D = \frac{3}{14}$				
$\alpha D = 56$	−2.5398	−0.0296	7.475	
$\alpha D = 28$	−2.5052	−0.0310	7.272	7.635

TABLE 1. Theoretical results for r, $s/\tilde{c}_0$ and c_0 for 1st mode

lowest mode has a maximum at the interface and corresponds to the interfacial internal wave. The next mode corresponds to the bulge-type wave. The solitary wave associated with the latter mode has been investigated by Kao & Pao (1979) for the case where $h_1 = h_2$. In the present investigation the bulge-type wave will not be pursued, and attention is confined to the lowest mode. The eigenvalue problem (2) is solved numerically in a normalized coordinate, with $\tilde{z} = z/D = 0$ at the bottom and $\tilde{z} = 1$ at the top, by finite-difference approximation and inversion of the resulting tridiagonal matrices (see Hildebrand 1968) for different values of h_1, h_2 and α^{-1}. The calculated values of c_0 for the lowest mode are shown in table 1, where 'two-layer' c_0 (hereinafter denoted by $\bar{c}_0$) refers to the linear interfacial long-wave speed for two discrete layers and is given by

$$\bar{c}_0 = \left(g \frac{h_1 h_2}{h_1 + h_2} \frac{\rho_2 - \rho_1}{\rho_2}\right)^{\frac{1}{2}}. \tag{3}$$

It can be seen that the effect of the finite transition pycnocline thickness is to decrease c_0 so that $c_0 < \bar{c}_0$. Such a decrease is significant for the pycnocline thickness in most laboratory experiments using salt solutions, and is very much more significant in the ocean pycnocline. Figure 2(*a*) shows a typical normalized eigenfunction, for the case $h_1/D = \frac{3}{14}$ and $\alpha D = 28$. Figure 2(*b*) shows a typical horizontal velocity profile associated with the vertical derivative of the eigenfunction in figure 2(*a*). It should be noted that away from the pycnocline the velocities become constant, independent of depth, with values proportional to D/h_1 and $-D/h_2$ in the upper and lower layers respectively. A distinctive aspect of the horizontal velocity profile is the shear at the pycnocline level. This shear is a characteristic feature of the internal solitary wave on the pycnocline that is absent in the classical free-surface solitary wave. It is expected to play an important and deciding role in wave-breaking when the amplitude of the wave becomes large or when solitary waves of depression shoal on a slope. This mechanism is also totally different from the breaking of a free-surface solitary wave.

Table 1 also presents the corresponding values of the parameters r and $s/\tilde{c}_0$, which are given by:

$$r = -\frac{3}{4} \frac{\int_0^1 \bar{\rho}' \phi_{\tilde{z}}^3 \, \mathrm{d}\tilde{z}}{\int_0^1 \bar{\rho}' \phi_{\tilde{z}}^2 \, \mathrm{d}\tilde{z}}, \quad s = -\frac{\tilde{c}_0}{2} \frac{\int_0^1 \bar{\rho}' \phi^2 \, \mathrm{d}\tilde{z}}{\int_0^1 \bar{\rho}' \phi_{\tilde{z}}^2 \, \mathrm{d}\tilde{z}}, \quad \tilde{c}_0 = \frac{c_0}{(gD)^{\frac{1}{2}}}, \tag{4}$$

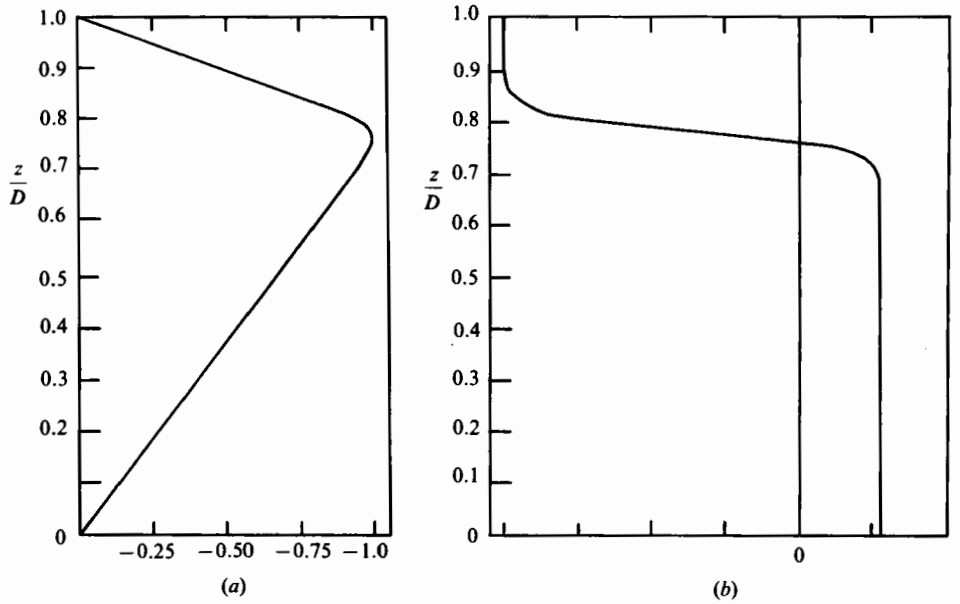

FIGURE 2. (*a*) Shape of normalized eigenfunction $\phi(\tilde{z})$. (*b*) Shape of horizontal velocity profile.

where $\overline{\rho}'$ is the specific gravity of the ambient stratification. (The values presented in table 1 are computed with $\overline{\rho}' = 1$, since we are within the Boussinesq approximation.) The knowledge of these parameters enables us to compute values of the characteristic length λ and wave speed c as follows:

$$\frac{\lambda}{D} = \left\{-\frac{6}{r}\frac{s}{\tilde{c}_0}\frac{D}{\overline{\eta}}\right\}^{\frac{1}{2}}, \tag{5}$$

$$c = c_0\left(1+\tfrac{2}{3}r\frac{\overline{\eta}}{D}\right), \tag{6}$$

where $\overline{\eta}$ is the amplitude of the solitary wave given by

$$\eta = \overline{\eta}\,\mathrm{sech}^2\frac{x-ct}{\lambda}. \tag{7}$$

The interfacial displacement η for the continuous pycnocline model can be shown to obey the following KdV equation:

$$c_0^{-1}\frac{\partial\eta}{\partial t}+\frac{\partial\eta}{\partial x}+\frac{2r}{D}\eta\frac{\partial\eta}{\partial x}+D^2s'\frac{\partial^3\eta}{\partial x^3} = 0, \tag{8}$$

where $s' = -s/\tilde{c}_0$. It is of interest to note that when $\alpha^{-1}\to 0$, i.e. when the pycnocline thickness tends to zero, the classical results for a discrete two-layer model are obtained. These results have always been obtained in the past from potential theory (see e.g. Segur & Hammack 1982). Thus, as $\alpha^{-1}\to 0$,

$$r = \frac{3}{4}\frac{h_1-h_2}{h_1h_2}D, \quad \frac{s}{\tilde{c}_0} = -\frac{1}{6}\frac{h_1h_2}{D^2}, \quad c_0 = \overline{c}_0, \tag{9}$$

within the Boussinesq approximation, leading to the well-known formulae

$$\lambda = \left\{\frac{4}{3}\frac{h_1^2 h_2^2}{(h_1-h_2)\,\bar{\eta}}\right\}^{\frac{1}{2}}, \quad c = \tilde{c}_0\left\{1+\frac{1}{2}\left(\frac{h_1}{h_2}-1\right)\frac{\bar{\eta}}{h_1}\right\}. \tag{10}$$

If the Boussinesq approximation is not invoked, then the limits, as $\alpha^{-1}\to 0$, are

$$\left.\begin{aligned} r = -\frac{3}{4}\frac{D(\rho_1 h_2^2-\rho_2 h_1^2)}{h_1 h_2(\rho_2 h_1+\rho_1 h_2)}, \quad \frac{s}{\tilde{c}_0} = -\frac{1}{6}\frac{h_1 h_2(\rho_2 h_2+\rho_1 h_1)}{D^2(\rho_2 h_1+\rho_1 h_2)}, \\ c_0^2 = \left\{\frac{g(\rho_2-\rho_1)\,h_1 h_2}{\rho_2 h_1+\rho_1 h_2}\right\}, \end{aligned}\right\} \tag{11}$$

so that

$$\lambda = \left\{\frac{4}{3}\frac{h_1^2 h_2^2(\rho_2 h_2+\rho_1 h_1)}{\bar{\eta}(\rho_2 h_1^2-\rho_1 h_2^2)}\right\}^{\frac{1}{2}}. \tag{12}$$

For a continuous stratification of the pycnocline type it is also of interest to relate the maximum displacement of an isopycnic to the disturbance velocity in the upper layer (here in the case where $h_1 < h_2$, only solitary waves of depression are possible, i.e. $\bar{\eta}$ is negative). After some manipulation, we find the relation

$$\frac{u_{\max}}{c_0} = \frac{|\bar{\eta}|}{h_1}, \tag{13}$$

where $u_{\max}$ is the maximum horizontal perturbation velocity at any level in the upper layer away from the pycnocline. It follows from (13) that $u_{\max}$ is larger or smaller than c_0, according to whether $|\bar{\eta}|$ is greater or less than h_1. Furthermore, from (6) it is seen that $|u_{\max}| \leqslant c$ if and only if

$$\frac{|\bar{\eta}|}{h_1} \leqslant \frac{1}{1-\left|\frac{2}{3}r\frac{h_1}{D}\right|}. \tag{14}$$

Since the waves are obtained as the solution along the channel of an initial step-like rectangular function with dimensional step-depth η_0 and step length L, we know from the now well-known inverse-scattering theory (see e.g.Ablowitz & Segur 1981; Whitham 1974) that the number N of solitons that will evolve is given by (see Messiah 1971)

$$N \leqslant \frac{S}{\pi}+1, \tag{15}$$

where, in the present context,

$$S = \left\{\frac{1}{3}\frac{r\tilde{c}_0}{s}\frac{\eta_0}{D^3}\right\}^{\frac{1}{2}} L. \tag{16}$$

It should be noted that in the two-layer limit, within the Boussinesq approximation, S becomes

$$S = \left\{\frac{3}{2}\frac{h_1-h_2}{h_1^2 h_2^2}\eta_0\right\}^{\frac{1}{2}} L. \tag{17}$$

3. Experimental set-up and procedure

Experiments were conducted in a long wave tank made of Plexiglas, measuring 0.6096 m (24 in.) deep, 0.3556 m (14 in.) wide and 9.144 m (30 ft) long. A watertight movable gate of the same width as the tank, functioning as the wave generator, was

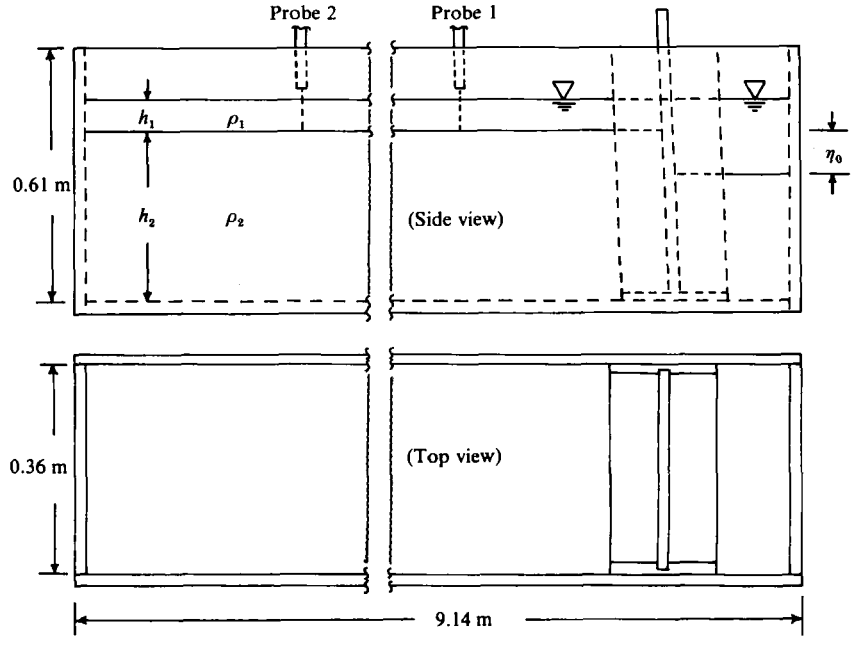

FIGURE 3. Experimental set-up, showing movable gate at right-hand end of tank.

installed near the upstream end of the tank (see figure 3). A configuration with shallow light water on top of a deeper layer of heavier (saltier) water was used. The depth of the light water behind the gate could be adjusted to exceed that in the main portion of the tank by any desired amount while keeping the free-surface level the same throughout the whole tank. The length of the trapped fluid could be varied by changing the location of the gate. In this way, a rectangular pool of light water of any desired depth and length could be trapped behind the gate. The gate could be lifted, at the initiation of an experiment, to allow this step-like rectangular light-water pool to propagate downstream. A schematic view of the experimental set-up is shown in figure 3. In Part 2 of this study a submerged shelf and slope were installed in the tank for the study of deformation, breaking and fission of the internal solitary wave. Four different measurement techniques were employed in the experiments.

(i) *Direct flow visualization*, by photographing the dyed-layer evolution.

(ii) *Hot-film anemometry*, using two hot-film anemometers (Thermosystem Models 1010A and 1050). The two hot-film probes were inserted at two different locations at the undisturbed pycnocline level (see figure 3). The outputs from the probes were recorded continuously on two separate strip-chart recorders running at a preselected speed. The probes measured the particle velocity of the fluid at these locations. Accurate calculation of the wave-propagation speed was made possible by measuring the arrival times of the peaks of the disturbance. The temporal velocity structure at the level of the probes and (for Part 2) the flow behaviour during the deformation, breaking and fission were measured quantitatively.

(iii) *Interface follower*. An interface follower that followed an isopycnic with great accuracy was used to measure the displacement waveform. The instrument consisted of a conductivity probe, which was slaved to move, through a servomechanism, with a predetermined conductivity layer corresponding to an isopycnic in the pycnocline. The instrument was developed by the Institut de Mécanique de Grenoble (the authors

wish to express their thanks to the Institute for the loan of the instrument) and has been described by Helal & Molines (1981). The isopycnic could be followed with a precision of 0.1 mm in height, and the response time was less than $\frac{1}{2}$ s. In the experiments the predetermined conductivity was chosen to be an isopycnic at approximately one-half of the pycnocline depth below the mid-depth of the pycnocline. The output from the interface follower was linear with the displacement, and was recorded continuously on the strip-chart recorder.

(iv) *Hydrogen-bubble technique.* In order to study the vertical shear structure during the passage of the wave in Part 2, the hydrogen-bubble technique was adopted to measure quantitatively the instantaneous velocity profile. The technique, utilizing the electrolysis of water to introduce hydrogen bubbles into the flow field, has been described extensively in the literature (see e.g. Davis & Fox 1967; Schraub *et al.* 1965). The bubble generator for the present study was made by stretching a fine platinum wire (0.03 cm in diameter) in a zigzag fashion between 2 vertical posts 5.08 cm apart in the cross-stream direction and extending through the depth of the flow. An electrical pulse was fed to the wire, and the hydrogen bubbles that were formed were swept off the wire by the flowing water. A slit-light box, equipped with high-intensity light source, with a slit size 3.7 cm wide and 76.2 cm long, was mounted on the top of the wave tank. The sheet of light defined a vertical plane in which the hydrogen bubbles were highly illuminated. The camera was located approximately 0.6 m away from the illuminated plane so that the bubbles could be highlighted. Synchronously with the excitation of the bubbles, the camera, equipped with a high-precision power winder, was triggered to shoot sequentially with an exact time interval of $\frac{1}{2}$ s. From the displacement of the hydrogen-bubble sheet in that time interval, the velocity profile throughout the depth of the flow was obtained.

In all experiments the tank was first filled with a layer of brine solution of density ρ_2, and a shallower and lighter layer of water of density ρ_1 was slowly filled on the top through a floating sponge dispenser. The density difference $\rho_2-\rho_1$ between these two fluids was fixed to be 0.01 g/cm^3. The total depth varied between 0.34 and 0.35 m. After filling, the fluid was allowed to stand for at least 2 h. The temperature of the fluid was found to be uniform and equal to the room temperature. The resultant density profile was measured by a conductivity probe or the interface follower and could be fitted by the hyperbolic tangent profile

$$\overline{\rho}(z) = \rho_0(1-\varpi \tanh \alpha z),$$

with α^{-1}, the representative half-pycnocline thickness, in the range 0.30–1.3 cm. A typical density profile is shown in figure 1. In the experiments a wide range of variation of the depths of the midpycnocline level was used. Indeed the midpycnocline level ranged from 0.95 to 7.6 cm below the free surface, so that the ratio h_1/D of the nominal upper-layer depth to the total fluid depth varied from 1:4.5 to 1:36.

4. Experimental results and discussion

4.1. *Wave generation*

Experiments were run by releasing various sizes of the step-like rectangular trapped light-water pool, with step length L and step depth η_0. Hot-film probes, placed beyond the sorting distance,† were used to record the number of waves that evolved from

† The sorting distance is the distance required for a set of ordered solitons to evolve from the initial disturbance. Hammack & Segur (1974) gave a simple prescription for its determination. Briefly, the sorting distance is given by $c_0\lambda/(c-c_0)$.

the initial disturbance. The processes that followed after the release included initial breaking, and the formation and propagation of the solitons. These processes were photographed.

Immediately following the opening of the gate, the trapped light-fluid pool began to move forward into the main portion of the channel, accompanied by some local vortices induced by the removal of the gate. Depending on the magnitude of the original step depth and length, the formation of the solitons was accompanied by different degrees of initial breaking, which restricted the maximum amplitude of the lead soliton.

The intensity and duration of the initial breaking appeared to increase with increase in η_0/L. The initial breaking, when it occurred, was due to the large shear at the interface. The initial breaking process, accompanying the lead soliton, ceased after the leading wave had travelled a distance of up to 2 m for the strongest case tested. For verifying the theoretical number of solitons, η_0/L was chosen to avoid such strong initial breaking, since this type of energy dissipation was not incorporated into the KdV theory.

The initial breaking is shown in figure 4 for three successive runs with increasing pycnocline thicknesses. It is seen that breaking was the strongest in the first run (top picture) after the layers were prepared and when the pycnocline was the thinnest. In the subsequent runs, under otherwise similar conditions, the breaking became weaker as the pycnocline was thickened by the previous experiment. The density profiles corresponding to the first and third runs are shown in figure 5, where the thickening of the pycnocline between these runs can be seen. The value of α^{-1} increased from 0.30 cm (0.12 in.) to 0.46 cm (0.18 in.) (the ratio h_1/D for the above runs was 1:36). This result suggests that breaking was due to the shear at the pycnocline. Stronger pycnoclinal shear due to a thinner pycnocline leads to more intense breaking for the same amplitude wave. A more systematic and detailed study of the rôle of shear on wave breaking is reported in Part 2 in conjunction with the breaking of shoaling waves.

The number of solitons that will evolve from the initial disturbances used in this study is given by (15) and (16) according to inverse-scattering theory and the present KdV model. We test the formula by conducting a set of experiments with $h_1/D = \frac{1}{14}$ and a total depth of 0.356 m (14 in.), but with a range of values of $|\eta_0|^{\frac{1}{2}}L$. In these experiments αD averaged about 28. A typical train of solitons as recorded by the strip-chart recorder is shown in figure 6. The upper trace is from an anemometer whose signal was not linearized, so that lower velocities were accentuated. The lower trace is from a linearized anemometer. A set of four ordered solitons is clearly discernible. Figure 7 (*a*) shows a photograph of the three leading solitons of a train of 8 solitons (theoretically). In this case the channel was too short for the solitons to sort themselves out totally before the lead soliton was reflected back from the downstream end of the tank. The result of this series of experiments is summarized in figure 8, where the number of solitons is plotted against the value of $|\eta_0|^{\frac{1}{2}}L$. The solid line is the theoretical lower bound and the dotted line is the theoretical upper bound using $\alpha D = 28$. The broken line is the lower bound using the two-layered model of (17). It is seen that the two-layered model overestimates the number of solitons, leading to considerable discrepancies with the experimental findings. Figure 7 (*b*) shows a single solitary wave. In most of the later experiments the initial condition was chosen so that only one, or at most two, solitary waves were produced.

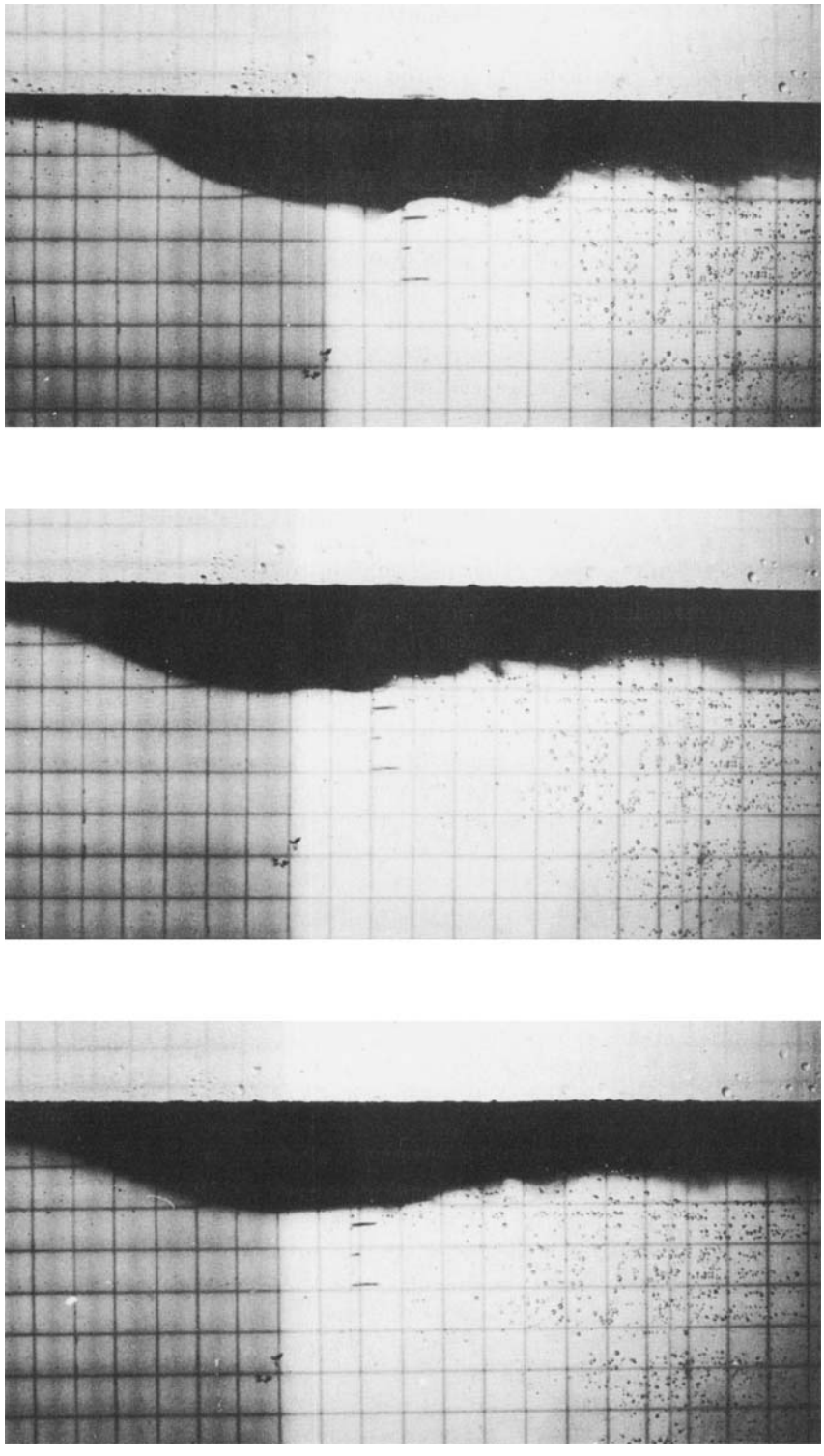

FIGURE 4. Initial breaking for three successive runs, showing effect of thickening pycnocline.

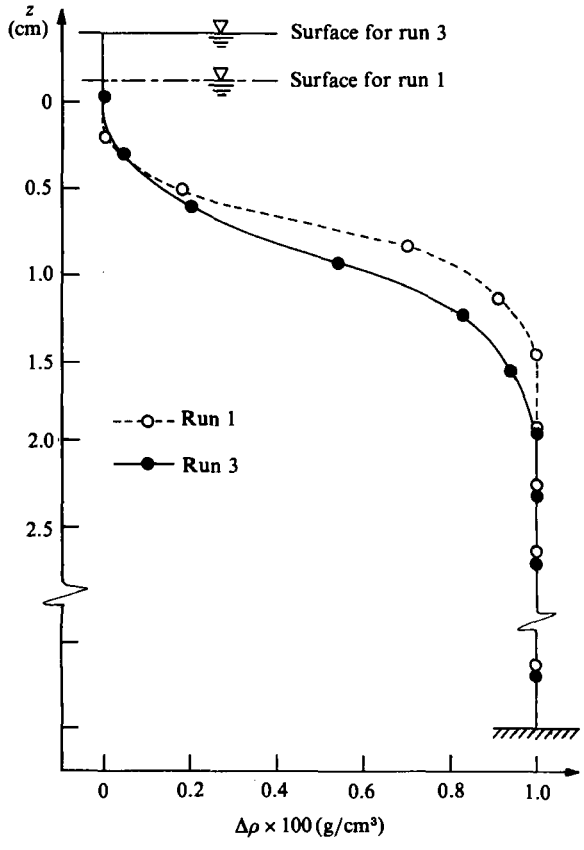

FIGURE 5. Measured density profiles for 1st and 3rd runs corresponding to figure 4.

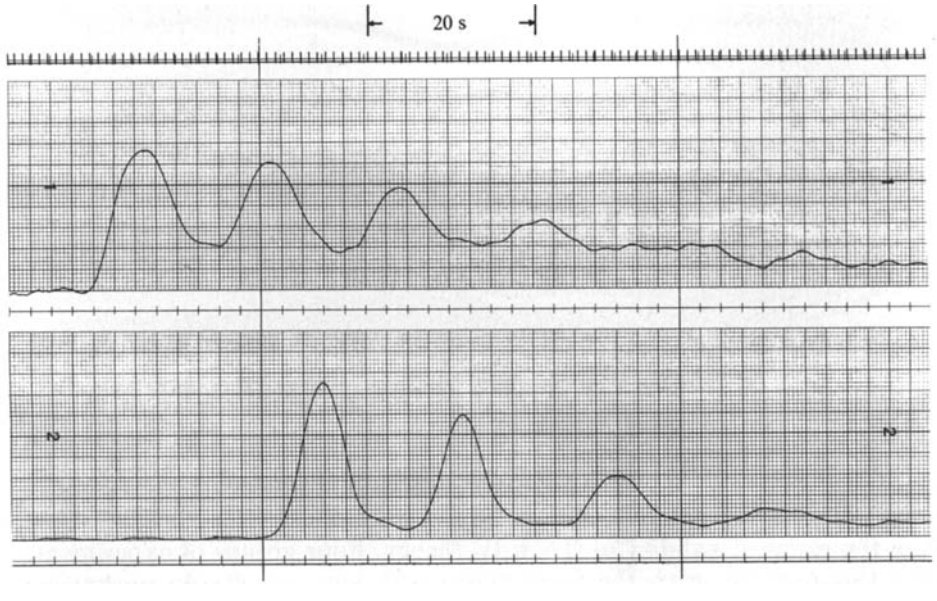

FIGURE 6. Typical train of solitons recorded by hot-film probes at two locations. Top trace is from a probe without linearizer, bottom trace is a linearized signal. The two probes are at a distance of 107 cm apart.

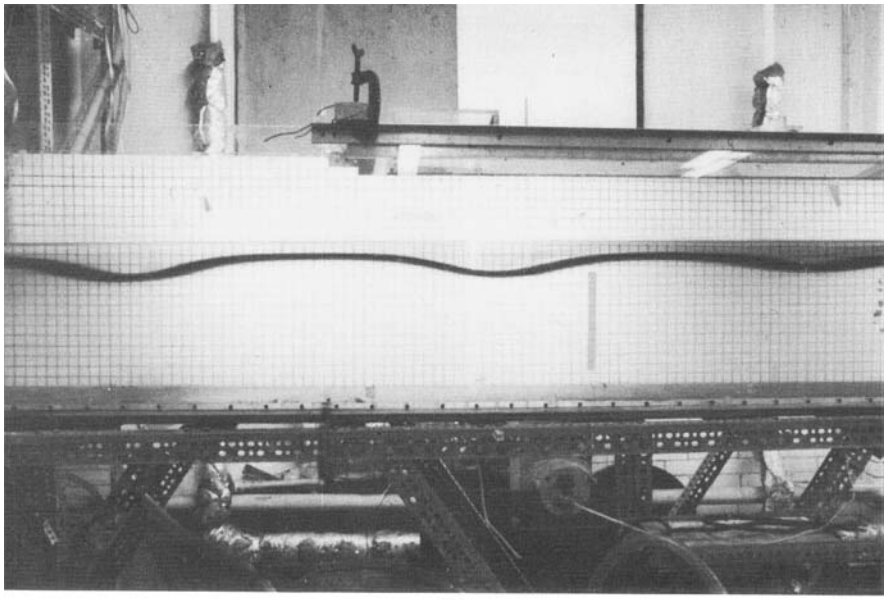

(a)

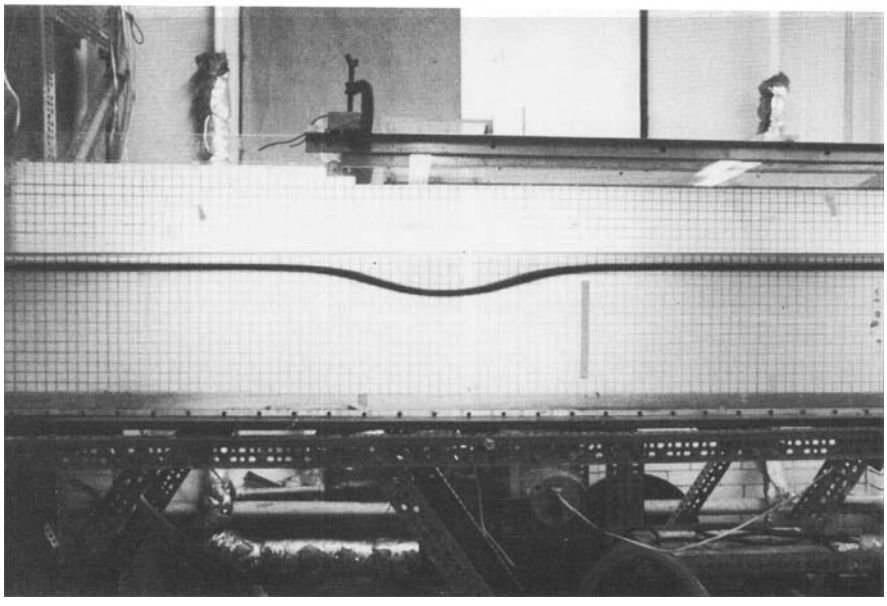

(b)

FIGURE 7. (a) Photo showing 3 leading solitons in a train. (b) A single soliton.

4.2. *Experimental evaluation of the validity and range of the KdV theory*

Various nominal layer-depth configurations were chosen for the experiments to explore the range of validity of the KdV theory. Four groups of experiments were run for this purpose, with the total fluid depth kept essentially unchanged. The nominal depths of the four groups are shown in table 2. It is seen that the ratio of $h_1 : D$ ranges from 1:4.5 to 1:36.

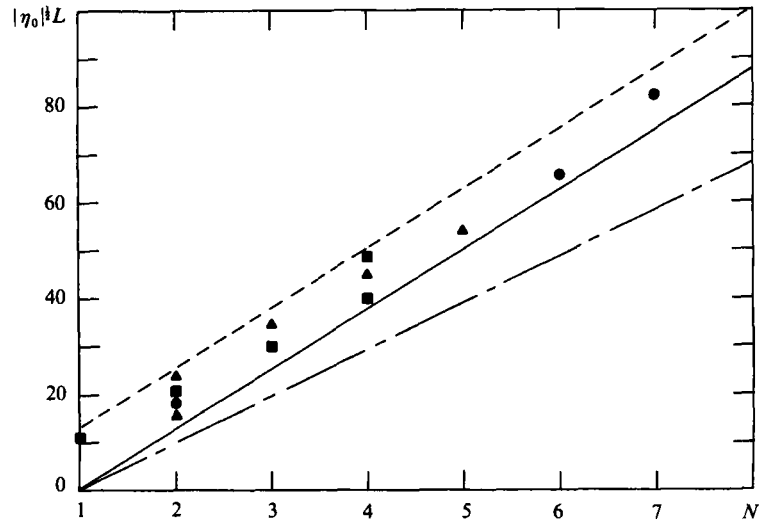

FIGURE 8. Comparison between measured number of solitons and theoretical predictions of the inverse-scattering theory: ——, theoretical lower bound; – – – –, theoretical upper bound; — — —, lower bound from two-layer theory.

Group	h_1 (cm)	h_2 (cm)	$D = h_1 + h_2$ (cm)	D/h_1	K
1	7.6	27.9	35.6	4.5	0.272
2	5.1	30.5	35.6	7	0.184
3	2.5	33.0	35.6	14	0.105
	1.6	33.0	34.6	22	0.067
4	1.5	33.0	34.5	23	0.063
	1.3	33.0	34.3	26	0.056
	0.95	33.0	34.0	36	0.040
Koop & Butler (1981)					
1	1.366	6.948	8.314	6	0.240
					0.195
					Boussinesq
2	1.366	47.87	49.236	36	0.040
					0.032
					Boussinesq

TABLE 2. Nominal depths and K-values in experiments

The output from the hot-film probe was recorded on the strip chart as a function of time. Initially only the hot-film probes were used. Subsequently, when the use of the interface follower became available its output was recorded similarly. Typical records from the hot-film probe and from the interface follower are shown in figures 9(*a*) and (*b*) respectively from two experiments in group 4. The wavelength of the disturbance was then calculated according to the definition

$$\lambda = \frac{1}{u_{\max}} \int_0^\infty u(x-ct)\,\mathrm{d}(x-ct), \tag{18a}$$

or

$$\lambda = \frac{1}{\bar{\eta}} \int_0^\infty \eta(x-ct)\,\mathrm{d}(x-ct), \tag{18b}$$

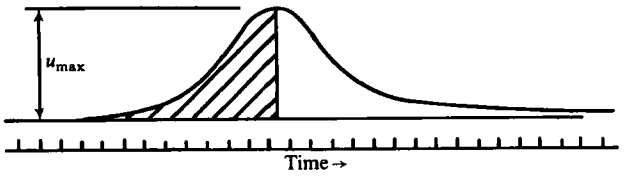

(a)

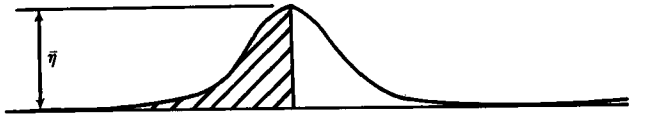

(b)

FIGURE 9. (a) Typical record of linearized hot-film probe output. (b) Typical record of linearized interface-follower output.

by using only the forward portion of the wave in a method similar to that used by Koop & Butler (1981), since the back portion of the wave is sometimes contaminated by the small-amplitude disturbances in the tail. The above definition is equivalent to taking the area of the shaded portion in figure 9 and dividing by the maximum value u_{max} or $\overline{\eta}$.

The wave speed or celerity of the wave was determined from the record of two probes, which were placed at a known distance apart, by measuring the time lag of the wave peak between the two probes. In all the experiments the time was determined to $\frac{1}{5}$ s. The experimental value of c_0, the linear long-wave velocity, was determined by measuring the wave speed of the soliton as its amplitude decreased during its travel over long distances and then linearly extrapolating to zero amplitude.

Three tests are used to test the range and validity of the KdV theory:

(i) the wave-length *vs.* amplitude relationship;

(ii) the incremental wave speed *vs.* amplitude relationship;

(iii) the sech^2 waveform profile.

Before proceeding to make these tests, we first examine the range of validity of the linear relationship between the maximum horizontal particle velocity u_{max} and the wave amplitude $\overline{\eta}$, by plotting u_{max}/c_0 against $\overline{\eta}/h_1$. The result of this comparison is shown in figure 10. It is seen that $u_{max}/c_0 = \overline{\eta}/h_1$ for $\overline{\eta}/h_1 < 1$, for all values of h_1/D tested. A progressive deviation was noted as $\overline{\eta}/h_1$ increased beyond 1. In the subsequent discussion the data on u_{max} were converted to wave amplitude, and no further distinction was made between hot-film-generated and interface-follower-generated amplitude data, except where it is specifically noted.

We now proceed to plot the wavelength *vs.* the amplitude for test (i), or, more precisely, to test the theoretical relationship given by (5). Equation (5) can be written as

$$\frac{\lambda}{D} = K\left(\frac{D}{\overline{\eta}}\right)^{\frac{1}{2}}, \tag{19}$$

where

$$K = \left|\frac{6}{r}\frac{s}{\tilde{c}_0}\right|^{\frac{1}{2}}. \tag{20}$$

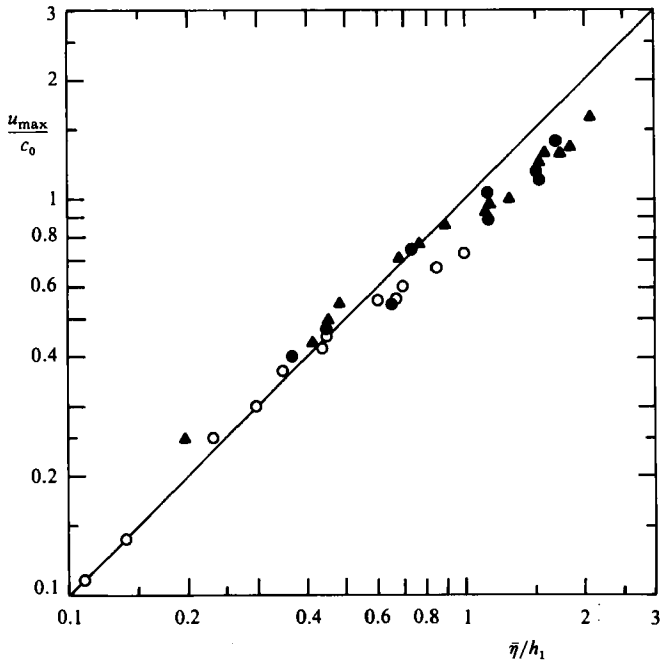

FIGURE 10. Intercomparison between hot-film reading and interface-follower reading: ●, $h_1/D = \frac{1}{20}$; ▲, $\frac{1}{14}$; ○, $\frac{1}{7}$.

Obviously, the best way to plot the data is to take the measured values of λ and $\bar{\eta}$ (or u_{max}) and plot λ/DK against $\bar{\eta}/D$ on a log–log plot. The theoretical KdV result is then represented by a single straight line with a negative slope of $\frac{1}{2}$ according to (19). The values of K in each group of experiments were obtained from the calculated values of r and $s/\tilde{c}_0$, with $\alpha D = 28$, and are listed in table 2. Also included in table 2 are the parameters for the two groups of experiments performed by Koop & Butler (1981). These experiments constitute the only other published experiments on the internal solitary wave with data that can be tested against the theory in this manner. The value of K for Koop & Butler's experiments are obtained from the two-layered model. The first value listed in each group is the exact value using (11). The second value (marked Boussinesq) is obtained from the conventional model using (9).

The result of plotting λ/DK against $\bar{\eta}/D$ from the present data is shown in figure 11. It is seen that the data from all 4 groups agree well with the KdV theory (shown in the figure as a solid line) to a remarkable degree of accuracy at small values of $\bar{\eta}/D$. We observe a systematic deviation from the theory at larger amplitudes. It is important to note that the deviation is independent of the depth ratio h_1/D. Thus the experimental results follow the KdV theory for the whole range of h_1/D tested; from 1:4.5 to 1:36. We also note that the data from $h_1/D = \frac{1}{14}$ to $\frac{1}{36}$ extend over one decade in the normalized amplitude $\bar{\eta}/D$ and shows exceptionally good agreement with the theory. These data, together with the data on wave speed and waveform to be presented subsequently in this paper, provide strong evidence that the KdV theory is valid for internal solitary waves in water of finite total depth.

The results of Koop & Butler (1981) are also indicated in figure 11 by dotted boxes. Both sets of results follow the inverse-square-root relationship of the KdV scaling law, but the case with $h_1/D = \frac{1}{36}$ was in considerable disagreement with the theoretical

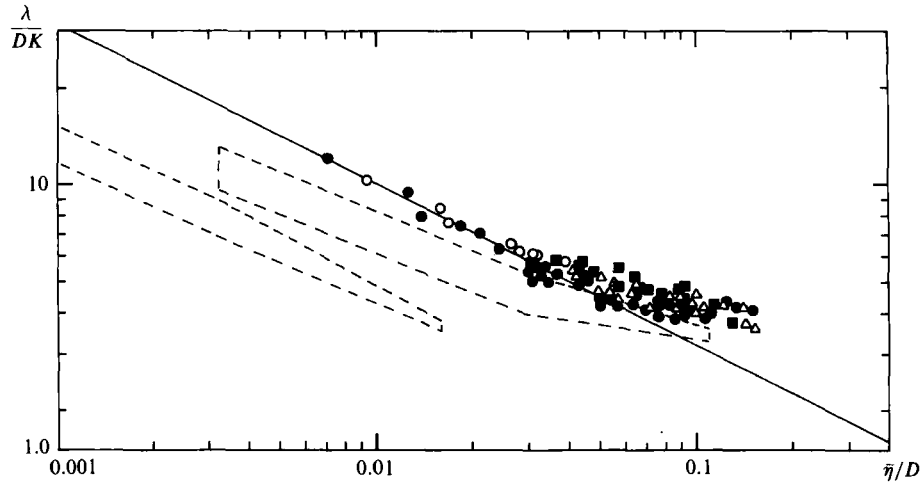

FIGURE 11. Dimensionless wavelength λ/DK versus wave amplitude $\bar{\eta}/D$: ○, $\frac{1}{36} < h_1/D < \frac{1}{18}$; ●, $h_1/D = \frac{1}{14}$; ■, $\frac{1}{7}$; △, $\frac{3}{14}$; ——, 1st-order KdV theory.

prediction. Indeed, as pointed out by Koop & Butler, the KdV theory overpredicts the experimental wavelengths by a factor of at least 2, perhaps because of the neglect of the real-fluid effects in the two-layer theory.

An additional comment that is relevant here is the use of $\bar{\eta}/D$ as the normalized amplitude parameter instead of $\bar{\eta}/h_1$ as used by Koop & Butler and others. $\bar{\eta}/D$ is the parameter dictated by the KdV theory, and we have seen that it correlated with the data very well. We found that if the data for λ/DK were plotted against $\bar{\eta}/h_1$ the correlation in terms of the systematic deviation due to large amplitude would be considerably poorer.

A second, equally definitive, test of the theory is to examine the wave-speed (or velocity) *vs.* amplitude relationship given by (6), or

$$\frac{\delta c}{c_0} = \tfrac{2}{3} r \frac{\bar{\eta}}{D}, \tag{21}$$

where δc is the increment in wave speed. Since δc is sensitive to the value of c_0, the measured value of c_0 must be used. We measured the wave speeds of the soliton as its amplitude decreased during its travel over several lengths of the tanks. The recorded value of c was then plotted against $\bar{\eta}$ or $u_{\max}$. In each case the relationship between c and $\bar{\eta}$ or $u_{\max}$ was found to be fairly precisely linear, especially when the amplitude became small. The straight line was extrapolated backwards to find the value of c at $\bar{\eta} = 0$ or $u_{\max} = 0$. The c thus determined was used as c_0 and was found always to be lower than the calculated values by approximately 15 % on the average. The data for $\delta c/c_0$ against $\bar{\eta}/D$ are shown in figure 12. The solid straight line is the theoretical result from (21). It is seen that the agreement is remarkably good, especially for lower values of $\bar{\eta}/D$, for all values of h_1/D. At larger amplitudes a systematic deviation from the linear relationship was again found. The results indicate that the increment in wave speed approaches an asymptotic limit of $\delta c = 0.1rc_0$ for $\bar{\eta}/D$ approaching 0.2.

A final and third test of the theory is to plot the waveform and check against the sech^2 distribution. For comparison the Lorentzian distribution will also be exhibited. We do this by demanding that the data fit both theoretical curves at two points. These

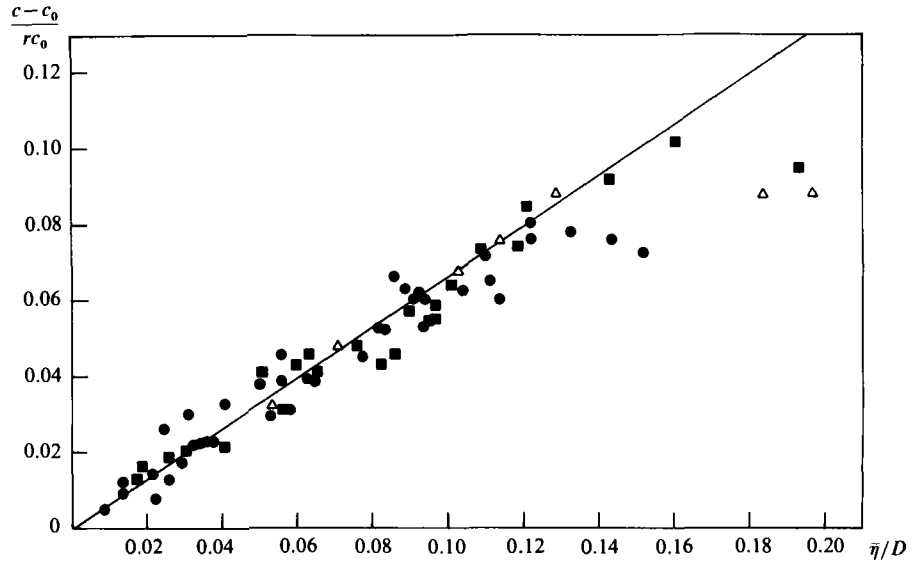

FIGURE 12. Dimensionless incremental wave speed $\delta c/c_0 r$ versus wave amplitude $\bar{\eta}/D$: ●, $h_1/D = \frac{1}{14}$; ■, $\frac{1}{7}$; △, $\frac{3}{14}$; ——, 1st-order KdV theory.

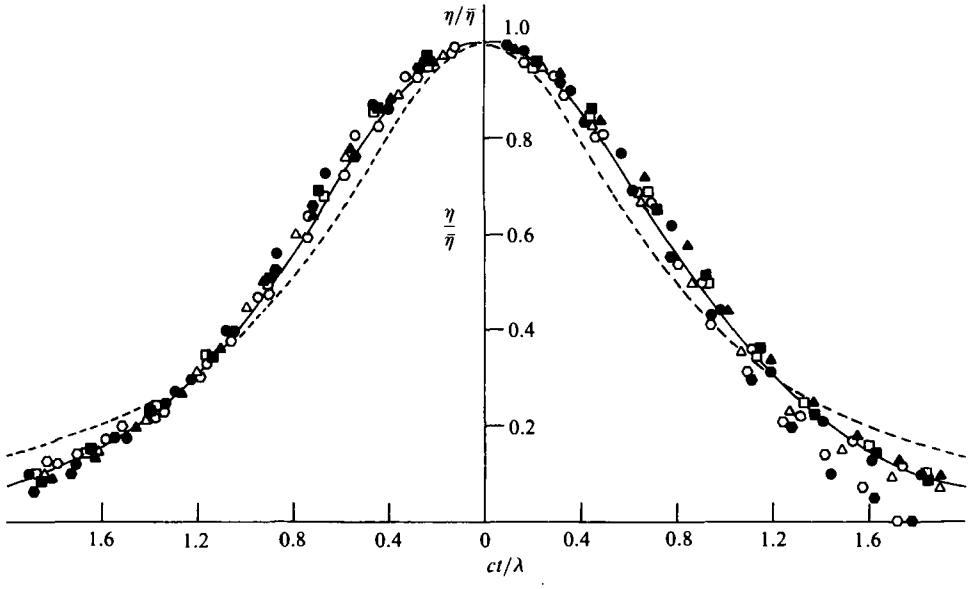

FIGURE 13. Normalized wave-amplitude *vs.* time (waveform): ——, sech^2 of KdV theory; – – – –, Lorentzian; ●, $h_1/D = \frac{1}{18}$; ○, $\frac{1}{21}$; ▲, $\frac{1}{14}$; △, ■, □, $h_1/D = \frac{1}{7}$; but with different amplitudes; ●, ⬡, $h_1/D = \frac{3}{14}$, but with different amplitudes.

two points are the point at the wave peak, and a point where the wave amplitude has dropped to 30.5% of the peak value. (This latter point was chosen since $\text{sech}^2 1.2 = 0.305$). The normalized plot of the wave profile based on the normalized isopycnic displacement amplitude $\eta/\bar{\eta}$ from the interface-follower data is shown in figure 13. The agreement with the sech^2 profile is truly excellent, particularly so for smaller values of h_1/D. The plot of the wave profile based on the velocity measurements

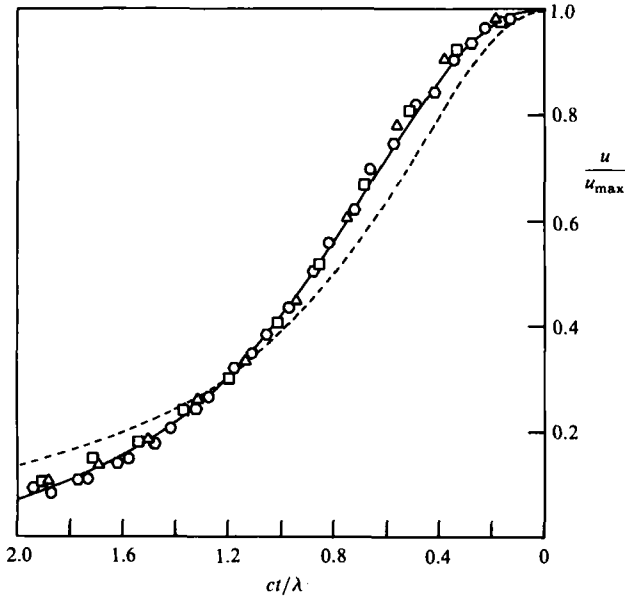

FIGURE 14. Normalized upper-layer horizontal velocity u/u_{max} versus time (waveform): ——, sech^2 of KdV theory; – – – –, Lorentzian; △, $h_1/D = \frac{1}{36}$; □, $\frac{1}{26}$; ○, $\frac{1}{23}$; ○, $\frac{1}{21}$.

of the hot-film anemometer is shown in figure 14 for small values of h_1/D. In this case, only the forward portion of the wave was plotted. The agreement is again seen to be superb.

From these exhaustive comparisons, we have confirmed that what are observed are truly the KdV solitary waves. Indeed the data represent a definitive confirmation of the KdV theory for internal solitary waves in a fluid of finite total depth, for a large range of values of the ratio of upper-layer thickness to total depth. We should also emphasize the inadequacy of the discrete two-layer model for the quantitative evaluation of data from a stratified fluid with a continuous pycnocline.

PART 2. WAVE SHOALING, INSTABILITY AND BREAKING ON A SLOPE

5. Shear instability

In Part 2 we investigate the evolution and breaking of the solitary wave as it shoals on a sloping bottom connecting the deeper region where the waves were generated to a shallower shelf region. For this purpose a slope and a shelf were installed in the wave tank used in Part 1. For comparison, the damping of the solitary wave when the slope and shelf were not present will also be included.

The water configuration in the present study continues to have a shallower upper layer, which is typical of ocean stratification. Since the solitary wave is a wave of depression, its geometrical relationship to the bottom slope is opposite to that of a free-surface wave. The breaking of solitary waves on the free surface has been known to occur when the particle velocity at the free surface at the crest exceeds the celerity of the crest. This condition is realized when the wave height reaches 70 % of the fluid depth, or $\overline{\eta}/h = 0.7$ (McCowan 1894). In a shoaling surface solitary wave this

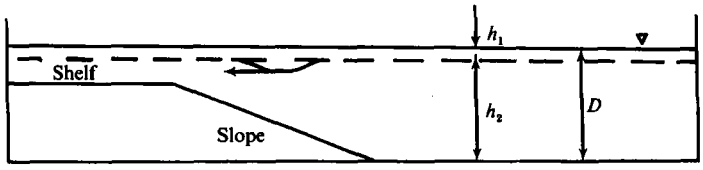

FIGURE 15. A schematic view of the shoaling experiment.

condition results in a spilling breaker similar to the breaking of progressive sinusoidal water waves.

The breaking of internal waves is rather different. The existence of a shear layer suggests the possibility of shear instability of the Kelvin–Helmholtz type (see e.g. Phillips 1966, p. 186). In the case of a shoaling internal solitary wave of the depression type not only is the existence of a strong shear layer important, but the geometrical configuration of the bottom relative to the wave now forces the intensification of the reverse flow in the lower layer to satisfy mass conservation during the passage of the wave up the sloping bottom. The shear across the pycnocline is therefore greatly intensified.

The possibility of shear instability in the pycnocline is therefore strongly suggested by the dynamically prominent vortex sheet at the interface. Miles (1961, 1963) and Howard (1961) have studied the stability of a stratified shear flow and have shown that a condition sufficient for the stability is that the local Richardson number $J(z) > \frac{1}{4}$ everywhere. The local Richardson number $J(z)$ is defined as

$$J(z) = -g\frac{\mathrm{d}\bar{\rho}}{\mathrm{d}z}\Big/\rho_0\left(\frac{\partial u}{\partial z}\right)^2, \tag{22}$$

where g is the acceleration due to gravity acting in the negative z-direction, $\bar{\rho}$ is the ambient stratification, ρ_0 is a reference density and u is the horizontal velocity. Though the flow is not necessarily unstable when $J(z) < \frac{1}{4}$, many examples of simple shear flows (see e.g. Miles 1963) do become unstable to some disturbances whenever $J(z) < \frac{1}{4}$. The criterion $J(z) < \frac{1}{4}$ is investigated in this study for the probable onset of instability pertaining to the shoaling of internal waves.

The fluid movement in the internal solitary wave is of course a case of unsteady shear flow. Relative to a fixed point in space, particle velocity is changing continuously with time. This type of unsteady shear motion induced by the propagation of the internal solitary wave has not yet been studied in detail theoretically. Nevertheless, it may be reasonable to assume that the stability criteria developed for steady basic flows would be relevant to the present study as long as the growth rate of an unstable disturbance is large compared with the rate at which the basic flow changes.

6. Experiments on shoaling solitons

The experimental procedures and techniques are the same as in Part 1. Several different slopes were employed in the shoaling experiments; but principally we present data for one with a 1:9 inclination and one with a 1:16 inclination. The projected horizontal lengths of the slope were 2.3 m and 4.06 m respectively. The nominal depth of the lower layer was 7.6 cm on the shelf and 33 cm in the deep-water side of the slope. In most of the shoaling experiments the nominal upper-layer depth was 2.54 cm, i.e. h_1/D in deep water was $\frac{1}{14}$. A schematic view of the shoaling experiment is shown in figure 15. The solitary wave was generated in the same manner

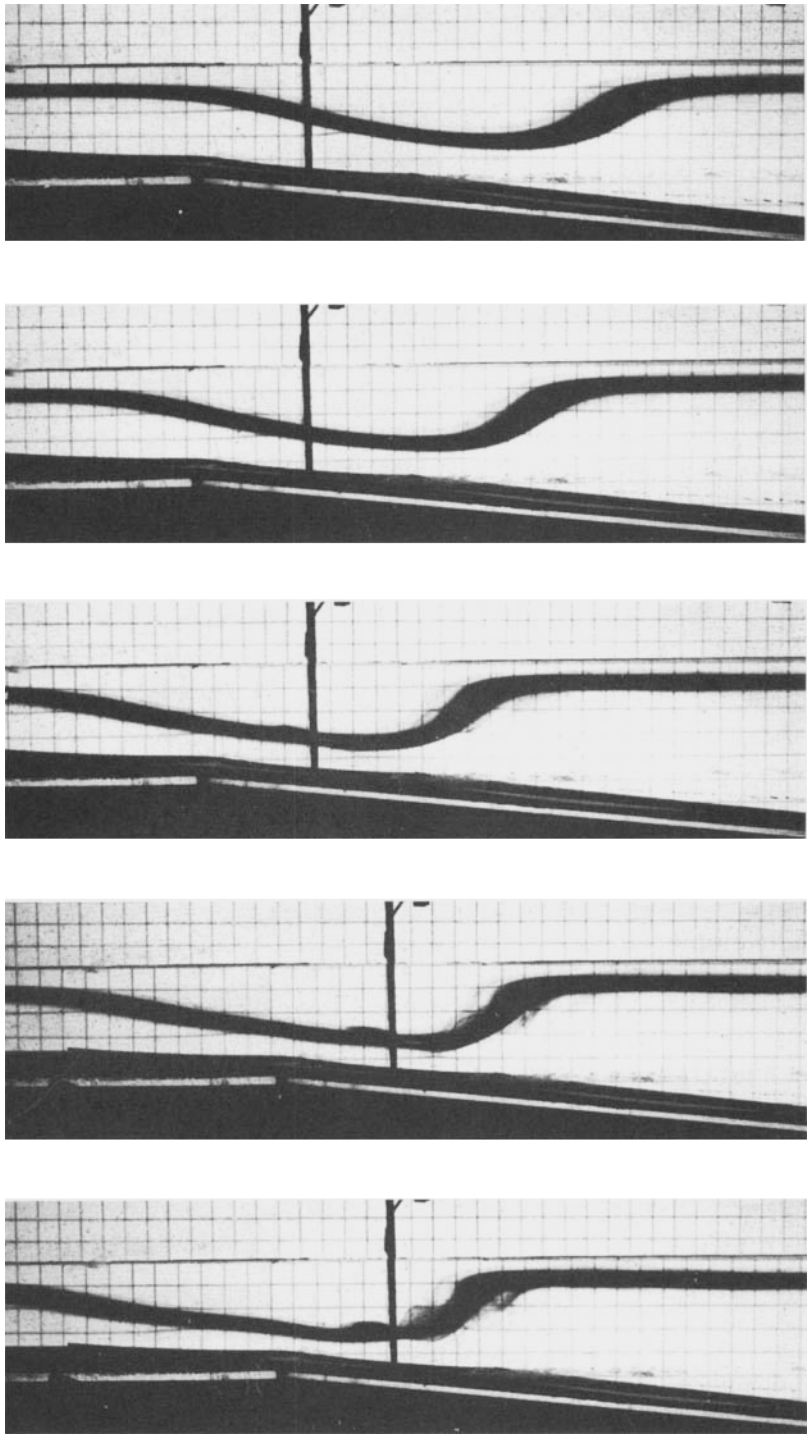

(*a*)

FIGURE 16(*a*). For description see page 41.

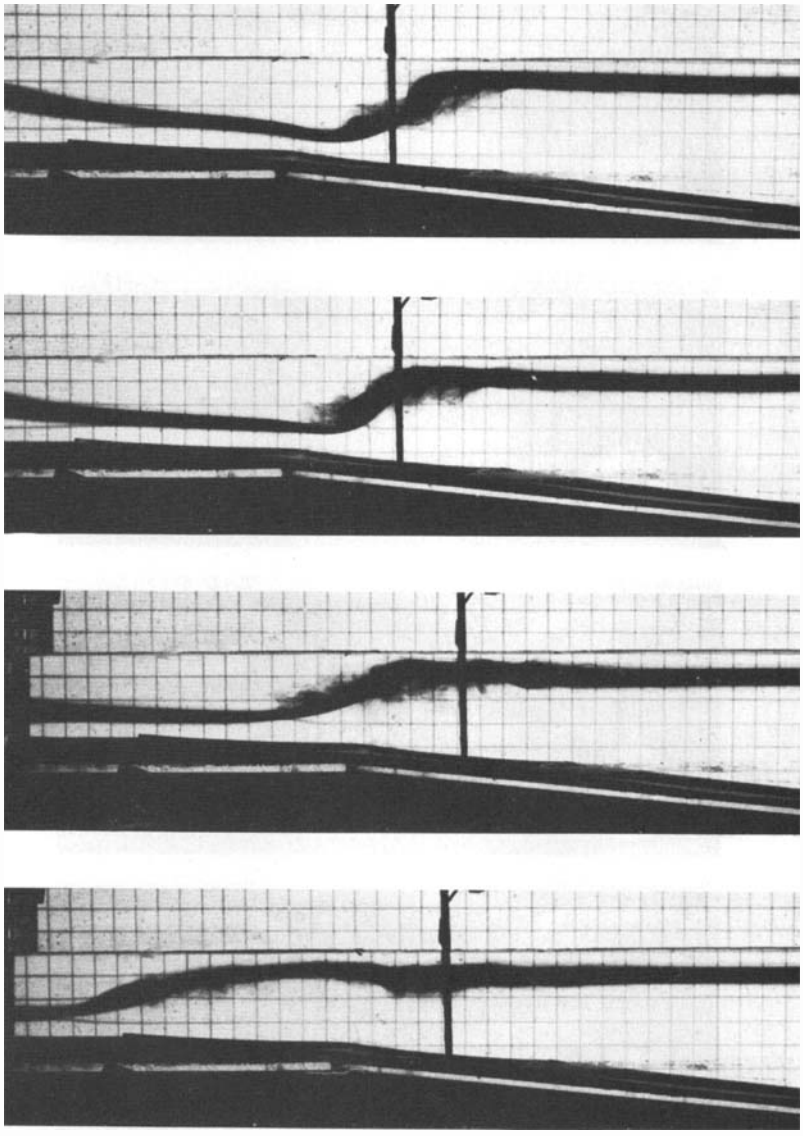

FIGURE 16(*a*) *continued*. For description see page 41.

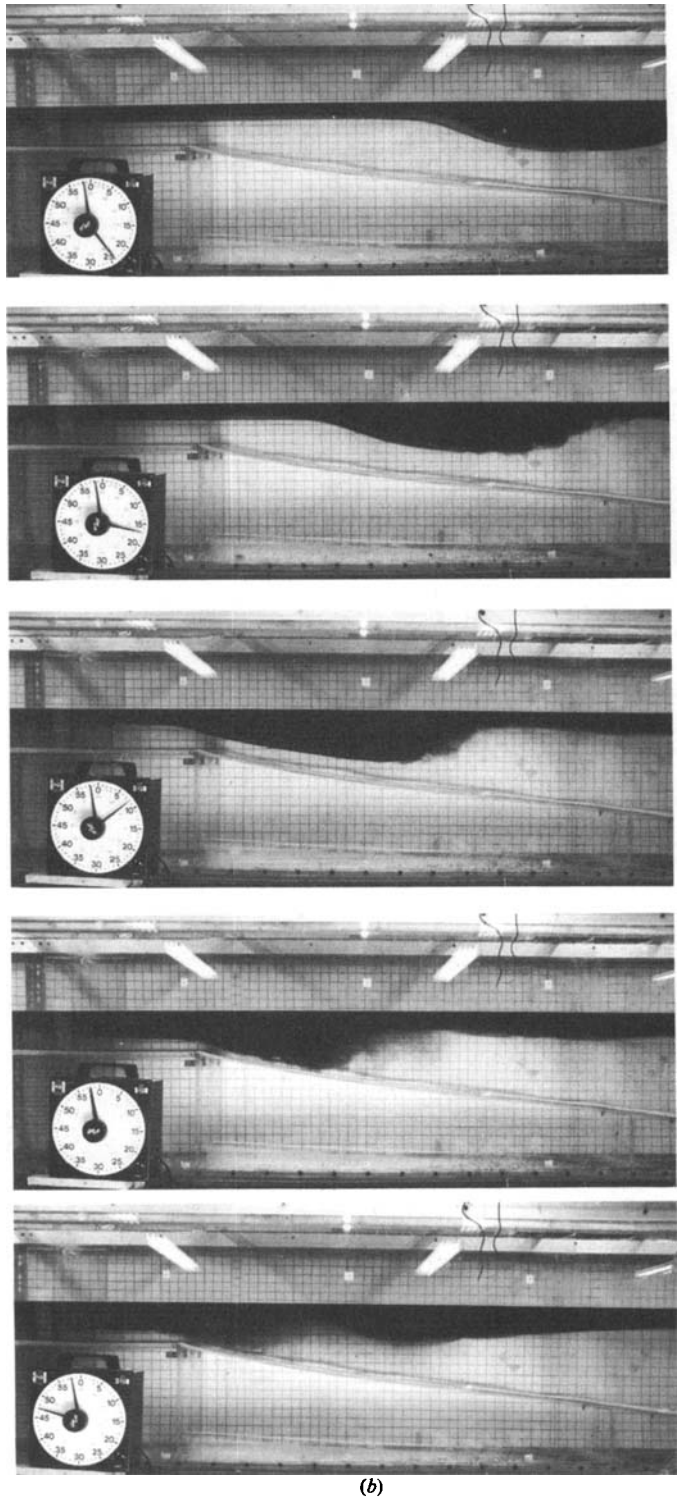

(*b*)

FIGURE 16(*b*). For description see facing page.

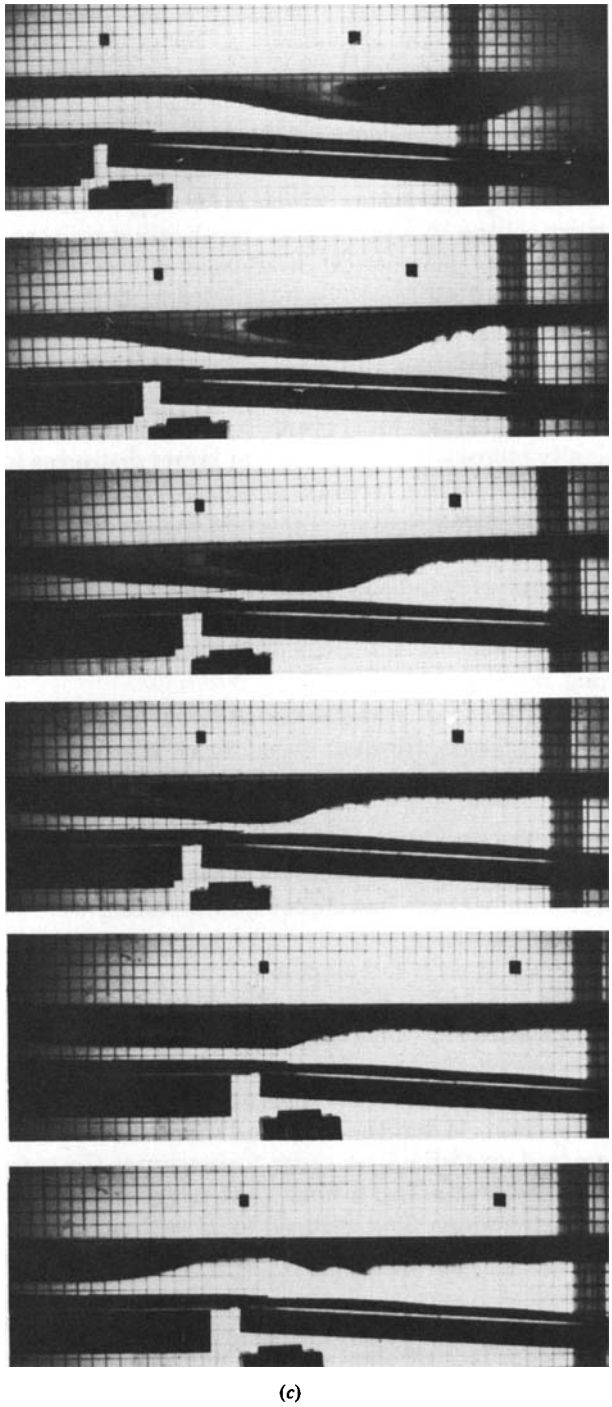

(*c*)

FIGURE 16. Sequences of photographs showing various stages of evolution and breaking of a shoaling internal solitary wave: (*a*) for a 1:9 slope and $\eta_0 = 11.4$ cm; (*b*) 1:7.5 slope and $\eta_0 = 15.2$ cm; (*c*) 1:16 slope and $\eta_0 = 12.7$ cm.

as that described in Part 1 by releasing a pool of trapped light water behind a sliding gate. As in Part 1, four different measurement techniques were employed in the experiments.

The solitary wave was generated in the deep-water part of the tank and allowed to propagate in deep water for at least 2 m before reaching the toe of the slope, so that the soliton was fully developed. (Note that the sorting distance was estimated to be less than 1 m for experiments in which $h_1/D = \frac{1}{14}$.) Care was taken to ensure that only one distinct soliton was present in the shoaling process. A second soliton, when and if generated, was generally so weak that it was sufficiently damped and well separated from the lead soliton to be insignificant. Different initial depths η_0 of the trapped light water were used to generate solitons of different amplitude. In order to provide a reference, the damping characteristics of these waves were measured first when the slope and shelf were not in place. It was found that the percentage of attenuation in water of constant total depth was 4.3 % m^{-1} from 3 m to 6 m from the gate, and gradually increased to 6.2 % m^{-1} at larger distances for $h_1/D = \frac{1}{14}$. (This percentage was found to decrease with increasing h_1/D.) The attenuation was also found to be less than the theoretical prediction of Leone, Segur & Hammack (1982) based on Keulegan's (1948) formulation of viscous decay of long linear surface waves. However, at a later stage of the decay processes when the wave had travelled over 16 m, the decay did follow the linear prediction rather precisely. This fact is attributable to the nonlinear characteristic of the wave, especially at the early stage of propagation along the wave tank.

We are now in a position to investigate the possible criterion for breaking for the shoaling internal solitary wave. Through visual observation of the dyed interface, we were able to make qualitative observations of the wave during the shoaling process on the slope for different values of η_0. (It should be noted that η_0 is the depth of the initial pool, and is not the amplitude of the wave. The amplitude of the wave is in general much less than η_0.) For $\eta_0 \leqslant 8$ cm no breaking or instability was observed. On the other hand, for $\eta_0 \geqslant 11$ cm instability and breaking were present for the 1:9 slope as well as the 1:16 slope.

The processes of breaking on a 1:9 slope and on a 1:16 slope are similar, but the appearance and extent are quite different. Breaking on a 1:9 slope excited more vigorous turbulence in a shorter duration than on a 1:16 slope. In general, before breaking, the wave was distorted so that the front of the wave became milder and roughly parallel to the inclined bottom. Also, the back of the wave became several times steeper than the front. When the distorted wave climbed further up, the shear at the interface increased accordingly in order to guarantee the conservation of mass. This increasing shear finally reached a limit that triggered interfacial instability in order to consume excess energy. The induced local turbulence due to breaking was located along the back of the wave, and sustained its intensity through the completion of the breaking event.

Figures 16(*a*)–(*c*) display three sequences of pictures in three experiments to demonstrate qualitatively the shear instability and breaking of the wave on different slopes. Figure 16(*a*) is a set of nine pictures taken for the wave of $\eta_0 = 11.4$ cm. The slope was 1:9. Pictures 1–8 were taken at approximate time intervals of 1–2 s, while picture 9 at the bottom was taken about 7 s after picture 8. The pictures show a steepening of the back of the wave and the associated shear instability, breaking and local turbulence. During the shoaling process the wave, which is of moderate amplitude and typical of most of our experiments, maintained its symmetric form to well beyond the midpoint of the slope. It then gradually felt the bottom with a

gradual steepening of the back of the wave. This is in distinct contrast with the shoaling process of the free-surface wave, when the waveform steepens in the front. This is, however, not surprising in view of the geometrical relationship between the wave of depression and the slope bottom. Concomitant with the steepening at the back, the density interface in the forward and main portion of the wave became nearly parallel to the bottom slope. This is seen in the top two pictures of figure 16(*a*). At this stage, interfacial shear disturbances began to appear, propagating towards the back of the main wave. These interfacial disturbances became stronger, as shown in the fourth and fifth pictures in figure 16(*a*). These disturbances subsequently burst into turbulence as the wave climbed over the top and seemingly squashed into the shallow shelf water. In the sixth and seventh pictures large-scale breaking in the lee was present. The intensity of the turbulence was seen to decay slowly for some period of time after the breaking, with the turbulent patch remaining near the location of the strongest breaking. No reflected wave was visible.

Figure 16(*b*) is for a case with $\eta_0 = 15.2$ cm on a slightly steeper slope of 1 : 7.5. (Note that increasing time in these pictures is indicated in the counterclockwise direction, and the inner (smaller) scale reads the seconds.) The top picture shows the stable large-amplitude wave. The second picture shows the wave undergoing strong shear instability 7 s later, with the shear billows growing to the back of the wave. The third picture shows that the forward portion of the solitary wave has adjusted to be nearly parallel with the bottom, and the back of the wave has steepened considerably with large-scale breaking and possible overturning in the lee of the wave. Picture 4 shows that, for this atypically large-amplitude wave, the turbulent patch of the broken wave touched the bottom. Picture 5 shows that a reflected wave was being formed.

Figure 16(*c*) shows a sequence of six pictures for a case with $\eta_0 = 12.7$ cm on a much gentler slope of 1 : 16. (These pictures were reproduced from coloured slides, and some details were obscured in the reproduction.) The breaking process occurred earlier when the wave reached the midslope region. Mild breaking of nearly constant intensity in the back of the wave was evident throughout the whole sequence. In comparison with the breaking on steeper slopes, which was rapid and vigorous, the process on the mild slope was more diffuse and took place over a much longer duration and distance, even though the phenomenon leading to breaking was much the same.

The particle velocity u in the upper layer was monitored by a hot-film probe. Figure 17 depicts the linearized output at two locations at $x_s^* = 66$ (two-fifths of the way up the slope) and $x_s^* = 143$ (near the top of the slope), where $x_s^* = x_s/h_1$ is the normalized horizontal distance measured from the toe of the slope. (The outputs were from two successive runs using the same probe.) These signals were for a larger-amplitude wave generated with $\eta_0 = 15$ cm on a 1 : 16 slope. (The total dimensionless length of this slope is 160.) A sign of a strong current is detected, with the first indication of a high-frequency turbulent patch immediately behind the crest (at a level of 2.5 cm below the surface). Visually, no clear pattern of breaking was observable for this wave at $x_s^* = 66$. The tendency towards instability gradually grew with the progression of the wave. Since the process of breaking is gradual and gentle, no specific location of breaking can be pinpointed. The maximum-velocity u_{max} signal at $x_s^* = 143$ involves a flat but rugged top indicating profuse turbulence. It shows that maximum particle velocity prevailed for a large portion of the breaking wave. Other aspects of the transformation of waves propagating on slopes of 1 : 9 and 1 : 16 will be discussed following the study of interfacial instability.

The foregoing investigations revealed that waves generated by releasing a step-pool of lighter fluid of various η_0 had shown consistent situations of instability on each

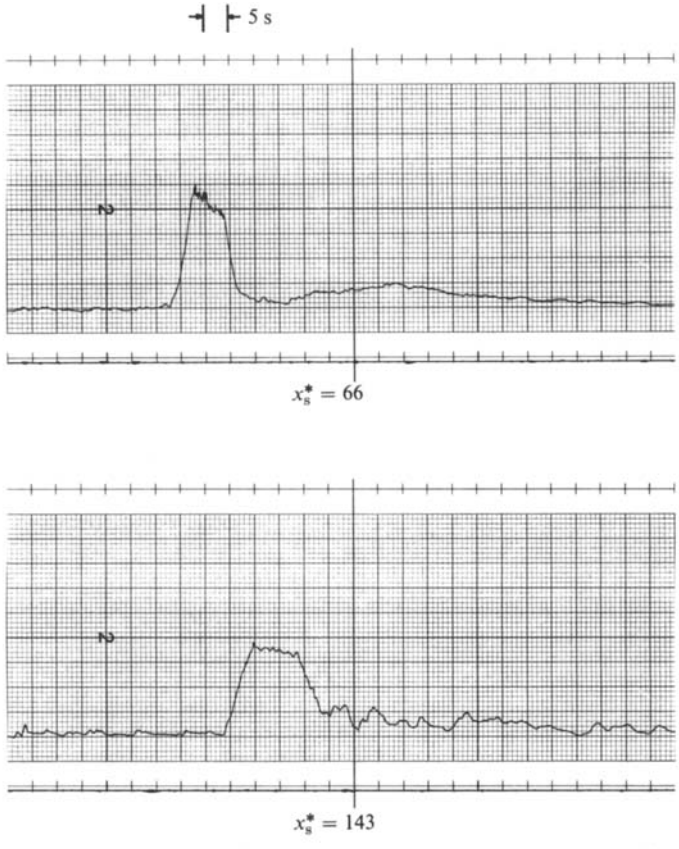

FIGURE 17. Linearized hot-film probe output at two locations on the slope, showing upper-layer particle velocity during breaking.

of the slopes, suggesting rather strongly the role of shear instability in the onset of the breaking process. It would therefore be of interest to investigate first the associated local Richardson number and compare it with Miles' criterion discussed in §5. Miles' criterion was developed for steady shear flow, but would most likely be applicable in unsteady situations if the growth rate of the unstable disturbance is large compared with the rate at which the basic flow changes.

It is known that, in a steady stratified fluid in shearing motion, the rate of growth of an unstable disturbance is proportional to the maximum shear rate (see e.g. Miles 1963). For a typical shoaling wave the maximum shear rate is

$$\left(\frac{\partial u}{\partial z}\right)_{\max} \approx \frac{c}{\Delta z} \approx \alpha c,$$

while the associated rate of change of the basic flow is n, where

$$n = \frac{\text{wave speed}}{\text{wavelength}} = \frac{c}{\lambda}.$$

Therefore

$$\left(\frac{\partial u}{\partial z}\right)_{\max} \Big/ n \sim \alpha c \Big/ \frac{c}{\lambda} = \alpha\lambda \gg 1.$$

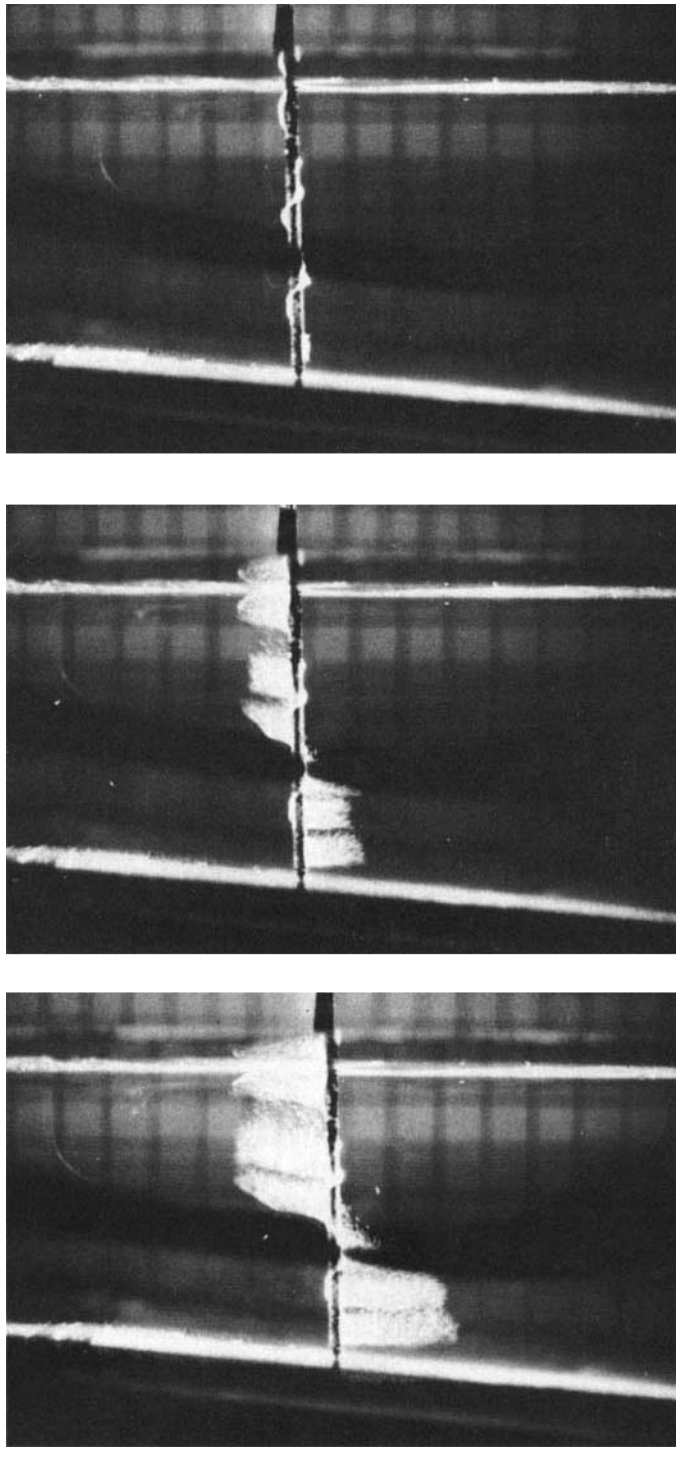

FIGURE 18. Photographs of illuminated hydrogen-bubble tracers during the passage of a solitary wave at successive times $\frac{1}{2}$ s apart.

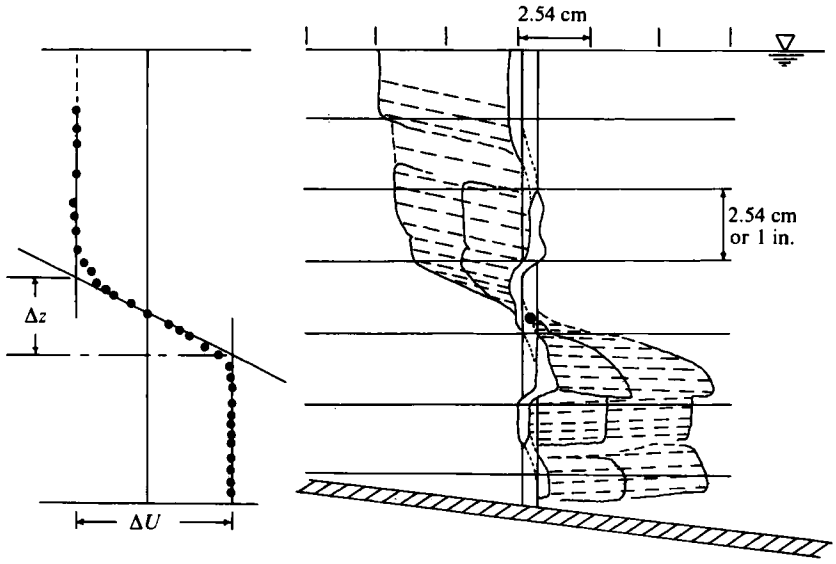

FIGURE 19. Construction of a shear profile during the passage of a solitary wave.

Generally, $\alpha\lambda$ is at least $O(10^2)$. Thus for all solitary waves on the pycnocline $(\partial u/\partial z)_{\max} \gg n$, i.e. Helmholtz instability occurs in a relatively short period of time compared with the rate of change of the basic flow. It is thus relevant to explore the breaking criterion for the solitary wave in terms of Miles' criterion for steady shear flow.

After several unsuccessful attempts using dye-injection techniques, the hydrogen-bubble technique was adopted. The method proved to be highly suitable for our purposes. During the experiment the hydrogen-bubble wiring system was inserted at the premarked location where the velocity profile would be investigated. An electric pulse was switched on to generate continuous streams of bubbles when the wave peak was still ahead of the premarked section by a few centimetres. Figure 18 shows three typical views of the illuminated hydrogen-bubble mist sheets. The first picture was taken immediately after the bubbles were generated ($t = 0$); the second and the third pictures were taken at successive instants of $t = 0.5$ s and $t = 1.0$ s respectively. The 'step' effect in the pictures, resulting from the zigzag wiring that went around the supporting rods, was very useful for tracing the paths of particles at each selected level. When the views of the bubbles were enlarged one at a time and superimposed on a large sheet of white paper by a slide projector, the velocity profile was constructed (see figure 19). It can be seen that particles in the mid-depth of the pynocline were stagnant. By using the velocity profile, conservation of mass flow was routinely checked and confirmed across the plane perpendicular to the fluid flow. As mentioned before, during the shoaling of the wave the reverse flow in the lower layer accelerated in order to conserve mass. This caused the shear to increase progressively as the wave travelled up the slope. It should be noted that, owing to the parallax effect, the background scale in figure 18 is smaller than the actual scale on the illuminated plane of the hydrogen bubbles. The actual scale was used to determine the values of Δz and ΔU.

In figure 2 a profile of horizontal velocity with $\alpha D = 28$ was plotted. From it we saw schematically that the thickness of the shear layer corresponds to $2\alpha^{-1}$, the

(*a*)

h_1/D	η_0 (cm)	On shelf	$x_s^* = 145$	$x_s^* = 70$	$x_s^* = 27$
$\frac{1}{14}$	7.6	—	0.37	0.45	0.45
	10.2	0.47	0.25	0.31	—
			0.26	0.33	
	12.7	—	0.22	—	0.31
			0.24		

(*b*)

h_1/D	η_0 (cm)	$x_s^* = 85$	$x_s^* = 0$
$\frac{1}{14}$	7.62	0.41	0.47
	10.2	0.29	0.37

TABLE 3. (*a*) Experimentally determined values of $J(z)$: (*a*) on a 1:16 slope and (*b*) a 1:9 slope

thickness of the pycnocline. This finding suggests that the local Richardson number can be expressed as

$$J(z) = \frac{g'(\Delta z)}{(\Delta U)^2}, \tag{23}$$

where g' is the reduced gravitational acceleration, Δz is the thickness of the shear layer and ΔU is the relative difference in the horizontal velocity of the corresponding shear flow (see figure 19). That $\Delta z = 2\alpha^{-1}$ was substantially confirmed in the present experiments. With Δz and ΔU determined experimentally, various values of $J(z)$ were calculated for waves propagating on both the 1:9 and 1:16 slopes. The results of the calculations of $J(z)$ are tabulated in table 3(*a*) for waves on a 1:16 slope, and in table 3(*b*) for waves on a 1:9 slope. Most values of $J(z)$ were sought for waves on a 1:16 slope, for which the breaking process was more gentle.

As we have observed in the present experiments, a wave generated with $\eta_0 = 10$ cm represented a marginal situation for interfacial stability on both 1:9 and 1:16 slopes. The amplitude of the wave at the toe of the slope was approximately 5 cm. The experimentally determined minimum values of $J(z)$ obtained from three independent experiments with $\eta_0 = 10$ cm were 0.25, 0.26 (on 1:16 slope) and 0.29 (on 1:9 slope), depending on the thickness of the pycnocline (later runs had thicker pycnoclines). A wave generated from $\eta_0 = 7.6$ cm (no breaking on both slopes) and waves generated from $\eta_0 = 12.7$ cm and 15.2 cm (breaking on both slopes) were also investigated. The minimum local Richardson numbers found for a wave generated from $\eta_0 = 7.6$ cm were 0.37 (on slope 1:16) and 0.41 (on slope 1:9). Waves generated from $\eta_0 = 12.7$ cm and $\eta_0 = 15.2$ cm both underwent gentle breaking on 1:16 slope during the shoaling process, and both had minimum local Richardson numbers smaller than the critical value of 0.25 (see table 3).

An overall review of the data in tables 3(*a*, *b*) suggests that the results are consistent, and that the local Richardson number indeed dominates the phenomenon of interfacial instability with a precise trend. Breaking was present at $x_s^* = 145$ on the 1:16 slope from a wave generated with $\eta_0 = 12.7$ cm or 15.2 cm, and the local Richardson number was indeed below $\frac{1}{4}$. It is thus concluded that Miles' criterion of the stability for the stratified shear flow (i.e. $J(z) > \frac{1}{4}$) is applicable to the present work, and $J(z) < \frac{1}{4}$ serves as a sufficient condition for the cause of interfacial instability for shoaling internal solitary waves.

It is also of interest to derive a simple predictive formula for internal solitary-wave

x_s^*	η_0 (cm)	(i) $\frac{D-x_s\tan\theta}{h_2-x_s\tan\theta}$	(ii) u_{max} (cm/s)	(iii) $(\Delta U)^2=[(i)\times(ii)]^2$	(iv) Calculated J	(v) Experimental J
			(*a*)			
145	7.6	1.254	6.48	65.8	0.38	0.37
	10.2		7.99	100.6	0.25	0.25
	12.7		9.07	129.0	0.19	0.23
70	7.6	1.116	6.48	52.2	0.48	0.45
	10.2		7.99	79.4	0.31	0.32
	12.7		9.07	102.6	0.24	—
27	7.6	1.088	6.48	49.7	0.50	0.45
	10.2		7.99	75.5	0.33	—
	12.7		9.07	97.4	0.26	0.31
			(*b*)			
85	7.6	1.281	6.48	68.8	0.36	0.41
	10.2		7.99	104.5	0.24	0.29
0	7.6	1.077	6.48	48.6	0.51	0.47
	10.2		7.99	73.7	0.34	0.37

TABLE 4. (*a*) Comparison between theoretical and experimental J: (*a*) on a 1:16 slope and (*b*) a 1:9 slope

breaking on a shoaling slope, based on (23), the lowest-order solitary-wave solution and Miles' criterion. Indeed, assuming that, for a slowly varying bottom, the pycnocline thickness $2\alpha^{-1}$ remains unchanged and the ratio of the upper- to lower-layer fluid velocity remains equal to the ratio of the nominal depths of the lower and upper layers during shoaling, the lowest-order solitary-wave solution gives

$$\Delta U = \frac{D-x_s\tan\theta}{h_2-x_s\tan\theta}u_{max}, \tag{24}$$

where u_{max} is the maximum horizontal velocity in the upper layer when the wave is in deep water, x_s is the horizontal distance measured from the toe of the slope, D is the total water depth in deep water, h_2 is the depth of the lower layer in deep water and θ is the angle of inclination of the slope to the horizontal. But, to lowest order,

$$u_{max} = \frac{\bar{\eta}}{h_1}c_0, \tag{25}$$

where $\bar{\eta}$ is the wave amplitude in deep water, h_1 is the depth of the upper layer and c_0 is the linear interfacial long-wave wave speed. Since $\Delta z = 2\alpha^{-1}$, (23) now becomes, on using (24) and (25),

$$J = \frac{2g'}{\alpha c_0^2}\left(\frac{h_1}{\bar{\eta}}\right)^2\left(\frac{h_2-x_s\tan\theta}{D-x_s\tan\theta}\right)^2. \tag{26}$$

Thus, given h_1, h_2 and $\bar{\eta}$, $J(z)$ can be calculated from (26) as a function of x_s, and the location where $J<\frac{1}{4}$ is the location of initial breaking.

Table 4 shows the values of J computed from (26) at the x_s^* locations along the slope corresponding to the experiments. The calculated values of J are listed in column (iv), and the values determined from the hydrogen-bubble experiments reported in tables 3(*a*, *b*) are shown in column (v) for both the 1:16 slope and the 1:9 slope. The

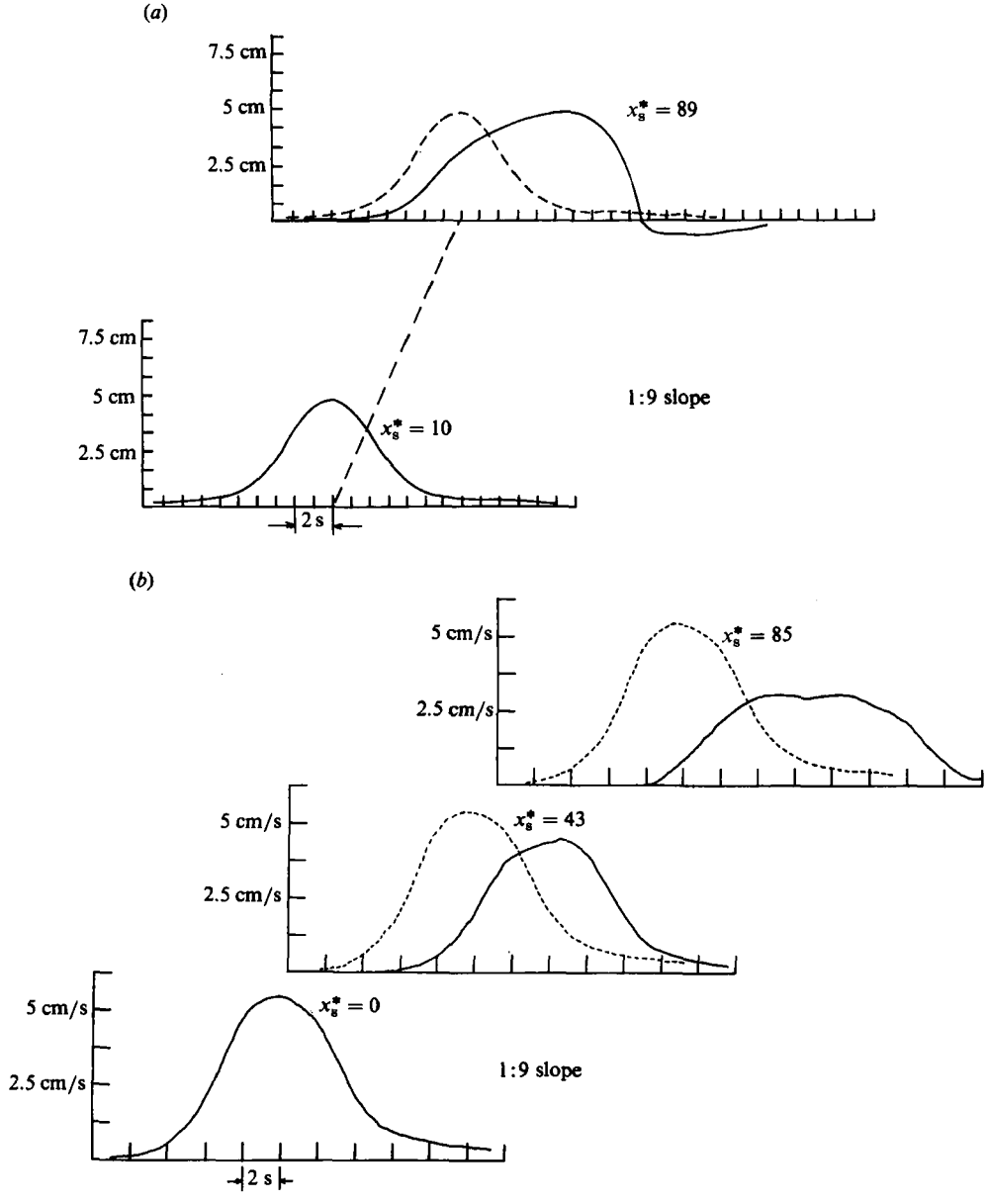

FIGURE 20. (*a*) Displacement profiles of the 'interface' as measured by an interface follower at $x_s^* = 10$ and $x_s^* = 89$ on a 1:9 slope during the passage of an internal soliton generated with $\eta_0 = 10.2$ cm. (The beginning of the slope corresponds to $x_s^* = 0$ and the end of the slope, $x_s^* = 90$.) (*b*) Upper-layer particle-velocity profile measured by a linearized hot-film probe at $x_s^* = 0$, $x_s^* = 43$ and $x_s^* = 85$ corresponding to figure 20(*a*).

agreement is seen to be remarkably good in view of the rather simple assumptions made in the derivation of (26).

The evolution of the wave profile and the evolution of the upper-layer particle velocity in the shoaling process were also quantitatively measured by means of the interface follower and the linearized hot-film anemometer at several locations along the slope. As in Part 1, the interface follower and the hot-film probe were inserted

in the vicinity of the pycnocline. For a set of different locations the experiment was repeated to generate the data for each location. For these measurements, experiments were conducted in which a step-pool of $\eta_0 = 7.62$ or 10.2 cm was released so that breaking would not occur on the slope.

Wave transformation on the 1:9 slope is shown in figures 20(*a*, *b*) for $\eta_0 = 10.2$ cm. Figure 20(*a*) shows the displacement profile of the interface as followed by the interface follower at $x_s^* = 10$ and $x_s^* = 89$. (The total normalized length of the slope is 90.) The dashed profile is that obtained from a separate experiment under otherwise identical conditions, but in water of constant total depth without the slope. It is seen that on this slope the deformation near the top of the slope is pronounced. The interface shows the characteristic steepening at the back of the wave as shown in the pictures in figure 16(*a*) for a larger-amplitude wave. A phase shift showing a delay in the arrival of the wave is also evident. Figure 20(*b*) shows the particle velocity in the upper layer for the same case, but from a different set of experiments. The particle-velocity profile in the upper layer experienced a very marked flattening and a collapse of the peak value concomitant with a strong increase in the lower-layer velocity. The velocity at $x_s^* = 85$, which is near to the top of the slope, shows a decrease, by the action of shear, in the front and middle portions of the wave. The peak velocity is markedly reduced by approximately $\frac{1}{3}$. The particle velocity towards the back of the wave is maintained, however. It can be seen that the duration of the wave was increased to accommodate the forward-moving fluid from the back of the wave. In this case instability was actually incipient. For larger-amplitude waves such as that in figure 16(*a*) the retardation of the peak velocity was more pronounced, and the forward motion of the fluid from the back of the wave could conceivably force the light upper fluid to be ejected downwards, inducing overturning and large-scale breaking in the final stage. It appears from these experiments that, for this to happen, the initial instability due to shear must occur first, and downward detrainment of light fluid is a manifestation of the growing instability. For $\eta_0 = 7.62$ cm the displacement profile was substantially unchanged from the constant-depth case, and the particle-velocity profile experienced only a slight flattening. No breaking was present.

Wave transformation on the 1:16 slope is depicted in figure 21(*a*, *b*) for $\eta_0 = 10.2$ cm. Figure 21 (*a*) shows the displacement profiles of the interface as followed by the interface follower at $x_s^* = 0$ and $x_s^* = 148$. (The total normalized length of the slope is 160.) The dashed profile is that obtained from a separate experiment under otherwise identical conditions, but in water of total constant depth without the slope. It is seen that, aside from a phase shift delaying the arrival of the wave, the wave profile is only slightly deformed, with only a slight steepening at the back of the wave. Figure 21 (*b*) shows the particle velocity in the upper layer at three locations $x_s^* = 0$, 37 and 102 for the same case, but from a different set of experiments. A similar phase shift was obtained, but there was a considerable flattening of the velocity profile compared with that in constant-depth water, in addition to a steepening at the back of the wave. There was an adjustment of particle velocity in the upper layer due to the large increase in particle velocity in the lower layer, even though the interfacial-displacement profile was not as sensitive to the presence of the bottom slope. The particle velocity at $x_s^* = 102$, which is just beyond the midpoint of the length of the slope, now already shows a collapse of the peak velocity similar to that which occurred in the previous case of the steeper slope near the top of the slope. In this case, breaking was again incipient, with J slightly larger than $\frac{1}{4}$. (Note that the amplitude of the wave in this run was smaller than that in the pictures shown in figure 16(*c*), where breaking was

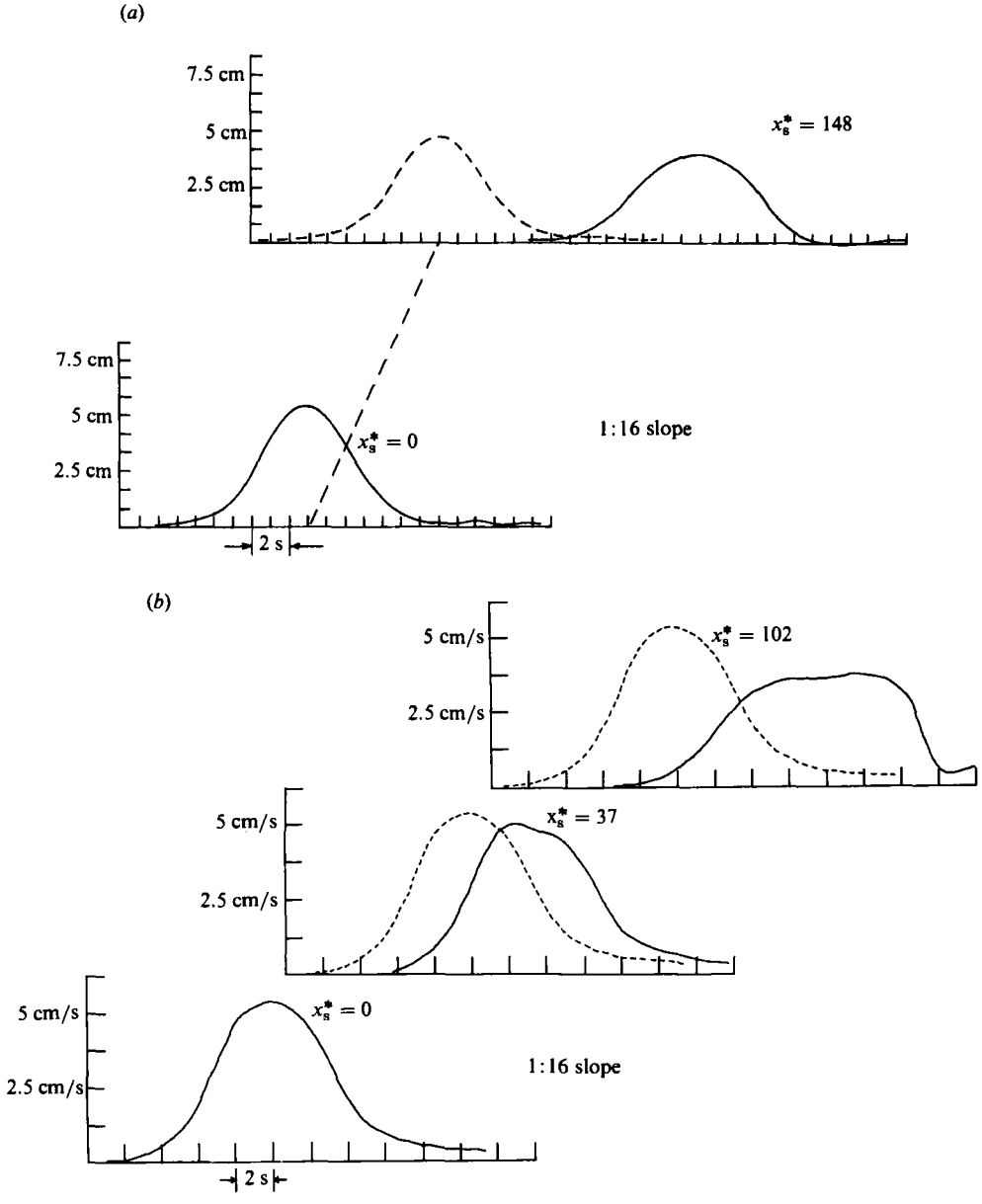

FIGURE 21. (*a*) Displacement profiles of the 'interface' as measured by an interface follower at $x_s^* = 0$ and $x_s^* = 148$ on a 1:16 slope during the passage of an internal soliton generated with $\eta_0 = 10.2$ cm. (The beginning of the slope corresponds to $x_s^* = 0$ and the end of the slope to $x_s^* = 160$.) The dotted profile is for the same wave at the same location without the sloping bottom. (*b*) Upper-layer particle-velocity profile measured by a linearized hot-film probe at $x_s^* = 0$, $x_s^* = 37$ and $x_s^* = 102$ corresponding to figure 21 (*a*).

occurring and for which J was less than $\frac{1}{4}$ beyond the midpoint of the slope.) For $\eta_0 = 7.62$ cm the results were similar to the corresponding case on the 1:9 slope, with no substantial changes in either the displacement or velocity profiles and no breaking.

When the wave reached the constant-depth region of the shelf without breaking, the wave appeared to be squashed into an elongated but symmetric waveform. This

flattened waveform was subject to considerable viscous action in the shallow shelf water. The waveform was subsequently shortened and the KdV profile recovered as the wave continued its travel on the shelf. However, by that time the wave had become extremely weak. No fission was observed even if the depth ratios of the shelf water were adjusted to values for which fission was predicted by the theory of Djordjevic & Redekopp (1978).

It thus appears that the evolution of the wave as it moved from deeper water over a slope to the shelf was either dominated by breaking when the amplitude was sufficiently large, or dominated by viscous damping on the shelf itself when the amplitude was small. When breaking was present a major portion of the energy was dissipated by the breaking process, although a portion of the wave energy was still transmitted onto the shelf in the form of a squashed elongated wave which subsequently suffered the same fate as the small-amplitude non-breaking wave. For the 1:16 and 1:9 slopes no reflected wave was detectable, for the typical amplitudes tested. For steeper slopes or very much larger-amplitude waves reflection was observed. However, these aspects are beyond the scope of the present study.

7. Concluding remarks

To summarize, we have found in this study that, regardless of the ratio of the upper- to lower-layer depth, internal solitons on the pycnocline in a fluid of total finite depth are governed by the KdV theory (see Part 1), that the solitons break by shear instability, that Miles' criterion for shear instability is applicable to the prediction of incipient instability and breaking of internal solitons on the pycnocline, that the local Richardson number of a shoaling wave can be simply calculated, and that the evolution of a soliton over a slope connecting the deep water to the shallower shelf water is dominated by real-fluid effects so that no fission was found for weak stratifications of Boussinesq fluids typical in nature.

This work was supported by the U.S. National Science Foundation under grant CEE83-08405. A portion of the work described in Part 2 was based on a dissertation presented by one of us (F.S.P.) in partial fulfilment of the Ph.D. degree requirement at the Catholic University of America. Thanks are also due to our colleague Dr H.-P. Pao for related discussions. The use of the interface follower was made possible through the courtesy of M. Chabert d'Hieres of the Institut de Mécanique, Grenoble, France.

REFERENCES

Ablowitz, M. J. & Segur, H. 1981 *Solitons and the Inverse Scattering Transform*. SIAM.

Apel, J. R. 1981 Update: internal waves in the Sulu Sea. *Bull. Am. Meteor. Soc.* **62**, 1061–1062.

Benjamin, T. B. 1966 Internal waves of finite amplitude and permanent form. *J. Fluid Mech.* **25**, 241–270.

Benjamin, T. B. 1967 Internal waves of permanent form in fluids of great depth. *J. Fluid Mech.* **29**, 559–592.

Benney, D. J. 1966 Long non-linear waves in fluid flows. *J. Maths & Phys.* **45**, 52–63.

Davis, W. & Fox, R. W. 1967 An evaluation of the hydrogen bubble technique for the quantitative determination of fluid velocities within clear tubes. *Trans. ASME* D: *J. Basic Engng* **89**, 771–781 (*ASME Paper* 66-WA/FE-21).

Djordjevic, V. D. & Redekopp, L. G. 1978 The fission and disintegration of internal solitary waves moving over two-dimensional topography. *J. Phys. Oceanogr.* **8**, 1016–1024.

HAMMACK, J. L. & SEGUR, H. 1974 The Korteweg–de Vries equation and water waves. Part 2. Comparison with experiments. *J. Fluid Mech.* **65**, 289–314.

HELAL, M. A. & MOLINES, J. M. 1981 Non-linear internal waves in shallow water. A theoretical and experimental study. *Tellus* **33**, 488–504.

HILDEBRAND, F. B. 1968 *Finite-Difference Equations and Simulations.* Prentice-Hall.

HOWARD, L. N. 1961 Note on a paper of John W. Miles. *J. Fluid Mech.* **97**, 115–127.

KAO, T. W. & PAO, H. P. 1979 Wake collapse in the thermocline and internal solitary waves. *J. Fluid Mech.* **97**, 115–127.

KEULEGAN, G. H. 1948 Gradual damping of solitary waves. *J. Res. Natl Bur. Stand.* **40**, 487–498.

KEULEGAN, G. H. 1953 Characteristics of internal solitary waves. *J. Res. Natl Bur. Stand.* **51**, 133–140.

KOOP, C. G. & BUTLER, G. 1981 An investigation of internal solitary waves in a two-fluid system. *J. Fluid Mech.* **112**, 225–251.

LEONE, C., SEGUR, H. & HAMMACK, J. L. 1982 Viscous decay of long internal solitary waves. *Phys. Fluids* **25**, 942–944.

LONG, R. R. 1956 Solitary waves in one- and two-fluid systems. *Tellus* **8**, 460–471.

LONG, R. R. 1965 On the Boussinesq approximation and its role in the theory of internal waves. *Tellus* **17**, 46–52.

MCCOWAN, J. 1894 On the highest wave of permanent type. *Phil. Mag.* (5) **38**, 351–358.

MESSIAH, A. 1961 *Quantum Mechanics*, vol. I. Wiley.

MILES, J. W. 1961 On the stability of heterogeneous shear flows. *J. Fluid Mech.* **10**, 496–508.

MILES, J. W. 1963 On the stability of heterogeneous shear flows. Part 2. *J. Fluid Mech.* **16**, 209–227.

OSBORNE, A. R. & BURCH, T. L. 1980 Internal solitons in the Andaman Sea. *Science* **208**, 451–460.

PHILLIPS, O. M. 1966 *The Dynamics of the Upper Ocean.* Cambridge University Press.

SCHRAUB, F. A., KLINE, S. J., HENRY, J., RUNSTADLER, J. & LITTELL, A. 1965 Use of hydrogen bubbles for quantitative determination of time-dependent velocity fields in low speed water flows. *Trans. ASME* D: *J. Basic Engng* **87**, 429–444 (*ASME Paper* 64-WA/FE-20).

SEGUR, H. & HAMMACK, J. L. 1982 Soliton models of long internal waves. *J. Fluid Mech.* **118**, 285–304.

WHITHAM, G. B. 1974 *Linear and Non-Linear Waves.* Wiley.